WRF-Chem simulation of aerosol seasonal variability in the San Joaquin Valley

Longtao Wu[1], Hui Su[1], Olga V. Kalashnikova[1], Jonathan H. Jiang[1], Chun Zhao[2], Michael J. Garay[1], James R. Campbell[3] and Nanpeng Yu[4]

1. Jet Propulsion Laboratory, California Institute of Technology, Pasadena, CA, USA

2. School of Earth and Space Sciences, University of Science and Technology of China, Hefei, Anhui, China

3. Naval Research Laboratory, Monterey, CA, USA

4. University of California, Riverside, Riverside, CA, USA

Submitted to *Atmospheric Chemistry and Physics*

March, 2017

____

Corresponding author address: Longtao Wu, 4800 Oak Grove Dr., Pasadena, CA 91109
E-mail: Longtao.Wu@jpl.nasa.gov

18 Highlights:

19 1. The WRF-Chem simulation successfully captures aerosol variations in the cold season in the

20   San Joaquin Valley (SJV), but has poor performance in the warm season.

21 2. High resolution model simulation can better resolve inhomogeneous distribution of

22   anthropogenic emissions in urban areas, resulting in better simulation of aerosols in the cold

23   season in the SJV.

24 3. Observations show that dust is a major component of aerosols in the SJV, especially in the

25   warm season. Poor performance of the WRF-Chem model in the warm season is mainly due

26   to misrepresentation of dust emission and vertical mixing.

Abstract

WRF-Chem simulations of aerosol seasonal variability in the San Joaquin Valley (SJV), California are evaluated by satellite and in-situ observations. Results show that the WRF-Chem model successfully captures the distribution, magnitude and variation of SJV aerosols during the cold season. However, aerosols are not well represented in the warm season. Aerosol simulations in urban areas during the cold season are sensitive to model horizontal resolution, with better simulations at 4 km resolution than at 20 km resolution, mainly due to inhomogeneous distribution of anthropogenic emissions and better represented precipitation in the 4 km simulation. In rural areas, the model sensitivity to grid size is rather small. Our observational analysis reveals that dust is a primary contributor to aerosols in the SJV, especially during the warm season. Aerosol simulations in the warm season are sensitive to parameterization of dust emission in WRF-Chem. The GOCART (Goddard Global Ozone Chemistry Aerosol Radiation and Transport) dust scheme produces very little dust in the SJV while the DUSTRAN (DUST TRANsport model) scheme overestimates dust emission. Vertical mixing of aerosols is not adequately represented in the model based on CALIPSO (Cloud-Aerosol Lidar and Infrared pathfinder Satellite Observation) aerosol extinction profiles. Improved representation of dust emission and vertical mixing in the boundary layer are needed for better simulations of aerosols during the warm season in the SJV.

1. Introduction

The San Joaquin Valley (SJV) in the southern portion of the California Central Valley is surrounded by coastal mountain range to the west and the Sierra Nevada range to the east. With cool wet winters and hot dry summers, the unique natural environment makes SJV one of the most productive agricultural regions in the world (SJV APCD, 2012 and references therein). However, SJV is also one of the most polluted regions in US due to its unique geographical location. Frequent stagnant weather systems are conducive to air pollution formation, while the surrounding mountains block air flow and trap pollutions. Large seasonal and spatial variation of aerosol occurrence and distribution are observed in the SJV. Although significant progress made to improving local air quality in past decades has been achieved through strong emission controls, PM2.5 (particulate matter with diameter ≤ 2.5 μm) concentrations in the SJV remain well above the national ambient air quality standards (NAAQS) threshold of 12 μg m^{-3} on an annual basis and 35 μg m^{-3} on daily basis, occurring mainly during the cold season. Improved understanding of the aerosol variability and impacts is needed to provide further guidance for emission control strategies in the SJV.

Air quality models are a useful tool to understanding the formation and evolution of aerosols and their impacts on air quality, weather and climate. However, it is quite challenging to accurately simulate aerosol properties (Fast et al., 2014). Fast et al. (2014) summarized the factors contributing to the errors in regional-scale modeling of aerosol properties. They include 1) emission sources; 2) meteorological parameterizations; 3) representation of aerosol chemistry; 4) limited understanding of the formation processes of secondary organic aerosol (SOA); 5) spatial resolution; and 6) boundary conditions.

67   As one of the advanced regional air quality models available presently to the community,

68   the Weather Research and Forecasting model with Chemistry (WRF-Chem) has been widely used

69   to study aerosols and their impacts on regional air quality, weather and climate (e.g., Misenis and

70   Zhang, 2010; Zhang et al., 2010; Zhao et al., 2010; 2013a, 2013b; 2014; Wu et al., 2011a, 2011b,

71   2013; Fast et al., 2012, 2014; Scarino et al., 2014; Tessum et al., 2015; Campbell et al., 2016; Hu

72   et al., 2016). For example, Fast et al. (2014) showed that WRF-Chem simulations at 4 km

73   horizontal resolution captured the observed meteorology and boundary layer structure over

74   California in May and June of 2010 and the spatial and temporal variations of aerosols were

75   reasonably simulated. Aerosol simulations by WRF-Chem are usually sensitive to both local

76   emission and long-range transport of aerosols from the boundary conditions provided by the global

77   Model for Ozone and Related chemical Tracers, version 4 (MOZART-4). With a similar model

78   set-up, Zhao et al. (2013b) conducted a one-year simulation at 12 km horizontal resolution and

79   found that the WRF-Chem model represented the observed seasonal and spatial variation of

80   surface particulate matter (PM) concentration over California. However, underestimation of

81   elemental carbon (EC) and organic matter (OM) were noticed in the model simulation, with weak

82   sensitivity to horizontal resolution.

83   In this study, we focus on simulating aerosol seasonal variability in the SJV, California

84   using similar model configurations as that used in Zhao et al. (2013b) and Fast et al. (2014). This

85   paper serves as the first step for future investigation of the aerosol impact on regional climate and

86   the water cycle in California. Previous studies have demonstrated that aerosols are better simulated

87   at higher model resolution (Misenis and Zhang et al., 2010; Qian et al., 2010; Stround et al., 2011;

88   Fountoukis et al., 2013). However, most regional climate studies are still performed with coarse

89   model resolutions (on the order of 10 km) due to the availability of computational resources. This

90 study will investigate the sensitivity of aerosol simulations to horizontal resolution and identify

91 optimal model physical choices for reasonable representation of aerosol variabilities in the SJV.

92   Another application of air quality modeling is to provide initial *a priori* fields for remote

93 sensing retrievals. The WRF-Chem model has been proposed as an input for retrieval algorithms

94 to be developed for the recently-selected NASA (National Aeronautics and Space Administration)

95 MAIA (Multi-Angle Imager for Aerosols) mission, which aims to map PM component

96 concentrations in major urban areas (including the SJV, a testbed for the MAIA retrieval algorithm

97 development). A significant challenge for aerosol remote sensing in retrieving spatial information

98 on specific aerosol types, especially near the surface, is caused by the lack of information on the

99 vertical distribution of aerosols in the atmospheric column and limited instrument sensitivity to

100 aerosol types over land. The WRF-Chem model will be used to provide near-real-time estimation

101 of particle properties, aerosol layer heights, and aerosol optical depths (AOD) to constrain the

102 instrument-based PM retrievals. A reasonable estimate of aerosol properties from WRF-Chem is

103 critical to ensuring retrieval speed and quality. Considering the sensitivity of WRF-Chem

104 simulations to various factors such as initial and boundary conditions, model parameterizations

105 and emission sources (e.g., Wu and Petty, 2010; Zhao et al., 2010, 2013a, 2013b; Wu et al., 2011a,

106 2015; Fast et al., 2014; Campbell et al., 2016; Morabito et al., 2016), careful model evaluations

107 are needed before the simulations can be used operationally for remote sensing retrievals. Thus,

108 this study is important for the development of MAIA retrieval algorithms, critical to the success

109 of the MAIA mission.

110   This paper is organized as follows. Section 2 describes observational datasets used for

111 model evaluation. Section 3 provides the description of the WRF-Chem model and experiment

112 setup. Model simulations and their comparison with observations are discussed in section 4.

113 Section 5 presents the conclusions.

2. Observations

2.1 Column-integrated Aerosol Optical Properties

116 AOD is a measure of column-integrated light extinction by aerosols and a proxy for total

117 aerosol loading in the atmospheric column. The Aerosol Robotic Network (AERONET) provides

118 ground measurements of AOD every 15 minutes during daytime under clear skies (Holben et al.,

119 1998), with an accuracy approaching ±0.01 (Eck et al., 1999; Holben et al., 2001; Chew et al.,

120 2011). The monthly level 2.0 AOD product with cloud screening and quality control is used in this

121 study. Ångström exponent (AE) is an indicator of aerosol particle size. Small (large) AE values

122 are generally associated with large (small) aerosol particles (Ångström, 1929; Schuster et al.,

123 2006). The AE between 0.4 μm and 0.6 μm is derived from AERONET observed AODs, and is

124 used to evaluate the model-simulated AE. For comparison with simulated AOD, AERONET AOD

125 is interpolated to 0.55 μm from 0.50 μm and 0.675 μm using the AE. In the SJV, only one

126 AERONET station at Fresno, CA (36.79°N, 119.77°W) has regular observations throughout the

127 California water year 2013 (WY2013) from October 2012 to September 2013.

128 The Multiangle Imaging Spectroradiometer (MISR) (Diner et al., 1998) instrument

129 onboard the Terra satellite has provided global coverage of AOD once a week since December

130 1999. The standard MISR retrieval algorithm provides AOD observations at 17.6 km resolution

131 using 16x16 pixels of 1.1 km x 1.1 km each. About 70% of MISR AOD retrievals are within 20%

132 of the paired AERONET AOD, and about 50% of MISR AOD falls within 10% of the AERONET

133 AOD, except in dusty and hybrid (smoke+dust) sites (Kahn et al., 2010). We use version 22 of

134 Level 3 monthly AOD product at 0.5° resolution in this study.

135   **2.2 Surface Mass Concentration**

136   Surface $PM_{2.5}$ speciation and PM_{10} (particulate matter with diameter $\leq$ 10 μm) data are

137   routinely collected by two national chemical speciation monitoring networks: Interagency

138   Monitoring of Protected Visual Environments (IMPROVE) and the $PM_{2.5}$ National Chemical

139   Speciation Network (CSN) operated by Environmental Protection Agency (EPA) (Hand et al.

140   2011; Solomon et al., 2014). IMPROVE collects 24-h aerosol speciation every third day at mostly

141   rural sites since 1988. The same frequency of aerosol speciation dataset was collected at EPA CSN

142   sites in urban and suburban areas since 2000. The observed organic carbon is converted to OM by

143   multiplying by 1.4 (Zhao et al., 2013b; Hu et al., 2016). Some precursors of aerosol pollutions

144   (such as NO_2 and SO_2) are observed hourly by EPA (data available at:

145   https://aqsdr1.epa.gov/aqsweb/aqstmp/airdata/download_files.html) and are used in this study.

146   Selected IMPROVE and EPA CSN sites used in this study are shown in Figure 1a.

147   **2.3 Aerosol Extinction Profile**

148   The aerosol extinction coefficient profile reflects the attenuation of the light passing

149   through the atmosphere due to the scattering and absorption by aerosol particles as a function of

150   range. Version 3 Level 2 532 nm aerosol extinction profiles derived from Cloud-Aerosol Lidar

151   with Orthogonal Polarization (CALIOP) backscatter profiles collected onboard the Cloud-Aerosol

152   Lidar and Infrared pathfinder Satellite Observation (CALIPSO) satellite are used (Omar et al.,

153   2009; Young and Vaughan, 2009). Seasonal mean profiles are derived for WY2013 based on the

154   methodology outlined in Campbell et al. (2012), whereby quality-assurance protocols are applied

155   to individual profiles before aggregating and averaging the data. We highlight that no individual

156   profiles are included in the averages if the CALIOP Level 2 retrieval failed to resolve any

157   extinction within the column, a potential issue to create bias that has recently been described by

158 Toth et al. (2017). Level 2 532 nm aerosol extinction data classify aerosols into 6 types: clean

159 marine, dust, polluted continental, clean continental, polluted dust and smoke. Dust and polluted

160 dust are distinguished in the averages in this study for their contribution to total extinction and the

161 vertical profile seasonally in the SJV.

162 **2.4 Meteorology**

163   AIRS (Atmospheric Infrared Sounder) onboard the Aqua satellite (Susskind et al., 2003;

164 Divakarla et al., 2006) has provided global coverage of the tropospheric temperature and moisture

165 at approximately 01:30 and 13:30 local time since 2002. AIRS retrievals have root-mean-squared

166 (RMS) error of ~1 K for temperature and ~15% for water vapor (Divakarla et al., 2006). Level 3

167 monthly temperature and moisture retrievals (version 6) at $1° \times 1°$ grid are used in this study.

168 Vertical gradient of equivalent potential temperature (θ_e) marks atmospheric stability and is

169 computed from temperature and moisture profiles observed by AIRS. Surface observations,

170 including air temperature, relative humidity (RH) and wind speed, are routinely collected at the

171 California Irrigation Management Information System (CIMIS; http://www.cimis.water.ca.gov/).

172 Precipitation used in this study is the Climate Prediction Center (CPC) Unified Gauge-Based

173 Analysis of Daily Precipitation product at $0.25° \times 0.25°$ resolution.

174 **3. Model Description and Experiment Setup**

175   The WRF-Chem model Version 3.5.1 (Grell et al., 2005) updated by Pacific Northwest

176 National Laboratory (PNNL) is used in this study (Zhao et al., 2014). This study uses the CBM-Z

177 (carbon bond mechanism) photochemical mechanism (Zaveri and Peters, 1999) coupled with the

178 sectional-bin MOSAIC (Model for Simulating Aerosol Interactions and Chemistry) aerosol

179 scheme (Zaveri et al., 2008) as the chemical driver. The major components of aerosols (nitrate,

180 ammonium, EC, primary OM, sulfate, sea salt, dust, water and other inorganic matter) as well as

181 their physical and chemical processes are simulated in the model. For computational efficiency,

182 aerosol particles in this study are partitioned into four-sectional bins with dry diameter within

183 0.039-0.156 μm, 0.156-0.625 μm, 0.625-2.5 μm, and 2.5-10.0 μm. Zhao et al. (2013a) compared

184 the impact of aerosol size partition on dust simulations. It showed that the 4-bin approach

185 reasonably produces dust mass loading and AOD compared with the 8-bin approach. The size

186 distribution of the 4-bin approach follows that of the 8-bin approach with coarser resolution,

187 resulting in ±5% difference on the ratio of $PM_{2.5}$-dust/PM_{10}-dust in dusty regions (more large

188 particles and less small particles). Dust number loading and absorptivity are biased high in the 4-

189 bin approach compared with the 8-bin approach.

190   Aerosols are considered to be spherical and internally mixed in each bin (Barnard et al.,

191 2006; Zhao et al., 2013b). The bulk refractive index for each particle is calculated by volume

192 averaging in each bin. Mie calculations as described by Ghan et al. (2001) are used to derive

193 aerosol optical properties (such as extinction, single-scattering albedo, and the asymmetry

194 parameter for scattering) as a function of wavelength. Aerosol radiation interaction is included in

195 the shortwave and longwave radiation schemes (Fast et al., 2006; Zhao et al., 2011). By linking

196 simulated cloud droplet number with shortwave radiation and microphysics schemes, aerosol

197 cloud interaction is effectively simulated in WRF-Chem (Chapman et al., 2009). Aerosol snow

198 interaction is implemented in this version of WRF-Chem (Zhao et al., 2014) by considering aerosol

199 deposition on snow and the subsequent radiative impacts through the SNICAR (SNow, ICe, and

200 Aerosol Radiative) model (Flanner and Zender, 2005, 2006).

201   The model simulations start on 1 September 2012 and run continuously for 13 months.

202 With the first month used for the model spin-up, our analysis focuses on WY2013 from October

203 2012 to September 2013. The model is configured with 40 vertical levels and a model top at 50

204   hPa. The vertical resolution from the surface to 1 km gradually increases from 28 m to 250 m. The

205   model center is placed at 38°N, 121°W, with 250 x 350 grid points at 4 km horizontal resolution

206   (referred to as "4km" hereafter; Table 1), covering California and the surrounding area. To test the

207   sensitivity of the aerosol simulations to horizontal resolution, one simulation with the same model

208   settings and domain coverage is conducted at 20 km horizontal resolution (referred to as "20km"

209   hereafter).

210   The physics parameterizations used in the simulations include the Morrison double-

211   moment microphysics scheme (Morrison et al., 2009), Rapid Radiative Transfer Model for General

212   circulation model (RRTMG) shortwave and longwave radiation schemes (Iacono et al., 2008),

213   Community Land Model (CLM) Version 4 land surface scheme (Lawrence et al., 2011). The

214   Yonsei University (YSU) planetary boundary layer (PBL) scheme (Hong et al., 2006) is used in

215   all of the simulations, except one sensitivity experiment that uses the ACM2 (Asymmetric

216   Convective Model with non-local upward mixing and local downward mixing; Pleim, 2007) PBL

217   scheme (referred to as "20km_P7" hereafter, Table 1). Subgrid convection, convective transport

218   of chemical constituents and aerosols, and wet deposition from subgrid convection are

219   parameterized using the Grell 3D ensemble cumulus scheme (Grell and Devenyi, 2002) in the 20

220   km simulations while convective processes are resolved in the 4 km simulations. The Interim

221   European Center for Medium-Range Weather Forecasts Re-Analysis (ERA-Interim; Dee et al.,

222   2011) serves as initial and boundary meteorological conditions for WRF-Chem. The MOZART-4

223   global chemical transport model (Emmons et al., 2010) is used for initial and boundary chemical

224   conditions. Fast et al. (2014) found that the MOZART-4 model overestimates aerosols in the free

225   troposphere over California, which is also found in one of our sensitivity experiments

226 ("20km_BC1" in the supplementary). Following Fast et al. (2014), the chemical initial and

227 boundary conditions from MOZART-4 are divided by two in all simulations except 20km_BC1.

228   Anthropogenic emissions are provided by US EPA 2005 National Emissions Inventory

229 (NEI05), with area-type emissions on a structured 4-km grid and point-type emissions at specific

230 latitude and longitude locations (US EPA, 2010). Nineteen gases (including SO_2, NO, NH_3 etc.)

231 are emitted, and aerosol emissions include SO_4, NO_3, EC, organic aerosols, and total $PM_{2.5}$ and

232 PM_{10} masses. Anthropogenic emissions are updated every hour to account for diurnal variability,

233 while its seasonal variation is not considered in the simulations. A sensitivity experiment with

234 2011 NEI emissions ("20km_NEI11" in the supplementary) does not produce significantly

235 different results from the 2005 NEI emissions. Biogenic emissions are calculated online using the

236 Model of Emissions of Gases and Aerosols from Nature (MEGAN) model (Guenther et al., 2006).

237 Biomass burning emissions are obtained from the Global Fire Emissions Database version 2.1,

238 with eight-day temporal resolution (Randerson et al., 2007) and updated monthly. Sea salt

239 emissions are derived from the PNNL-updated sea salt emission scheme that includes the

240 correction of particles with radius less than 0.2 μm (Gong et al., 2003) and dependence on sea

241 surface temperature (Jaeglé et al., 2011).

242   Following Zhao et al. (2013b), dust emission is computed from the GOCART (Goddard

243 Global Ozone Chemistry Aerosol Radiation and Transport) dust scheme (Ginoux et al., 2001) in

244 the 20km and 4km simulations. The GOCART dust scheme estimates the dust emission flux F as

245     $$F = CSs_p u_{10m}^2 (u_{10m} - u_t) \qquad ,$$

246 where C is an empirical proportionality constant, S is a source function for potential wind erosion

247 that is derived from 1° x 1° GOCART database (Freitas et al., 2011), s_p is a fraction of each size

248 class dust in emission, u_{10m} is 10-m wind speed and u_t is a threshold speed for dust emission.

249   As shown later, a significant amount of dust is observed in the SJV, whereas the GOCART

250   dust scheme produces little dust. Two sensitivity experiments at 20 km and 4 km horizontal

251   resolution (hereafter referred to as "20km_D2" and "4km_D2", respectively) are conducted by

252   switching the dust emission scheme to the DUST TRANsport model (DUSTRAN) scheme (Shaw

253   et al., 2008). The DUSTRAN scheme estimates F as

254          $$F = \alpha C u_*^4 \left(1 - \frac{f_w u_{*t}}{u_*}\right) \qquad ,$$

255   where C is an empirical proportionality constant, α is the vegetation mask, u_* is the friction

256   velocity, u_{*t} is a threshold friction velocity and f_w is the soil wetness factor. The C value in both

257   GOCART and DUSTRAN is highly tunable for different regions. The original C values, $1.0 \ \mu g \ s^2$

258   m^{-5} in GOCART (Ginoux et al., 2001) and 1.0×10^{-14} g cm^{-6} s^{-3} in DUSTRAN (Shaw et al., 2008),

259   are used in this study.

4. Model Simulation Results

261   Shown in Fig. 1a, our model domain includes three urban sites (Fresno, Bakersfield and

262   Modesto) and two rural sites (Pinnacles and Kaiser) where surface measurements of aerosols are

263   available. Because aerosols properties and model performance are similar at all urban sites, our

264   discussion is focused on the results at Fresno and the simulations for other urban sites are provided

265   in the supplementary materials. Model simulations in the rural areas are presented in the last

266   subsection.

4.1 Sensitivity to Horizontal Resolution

268   Figure 1 features daily mean anthropogenic $PM_{2.5}$ emission rates used in the 20km and

269   4km simulations, respectively. Although both emission rates are derived from the 4 km NEI05

270   dataset, localized high emission rates with sharp gradients are evident in urban areas from the 4km

271   simulation (Fig. 1b). The 20km simulation exhibits lower emission rates at the urban areas with

272   weaker gradients due to the reapportionment process (Fig. 1a). As precipitation is an important

273   process that removes aerosols, we examine the simulated precipitation for the 20km and 4km runs

274   and find that the 20km simulation produces 51% more precipitation, although the domain averaged

275   precipitation is lower in the 20km run than the 4km run (Fig. 2a).

276   Consistent with higher emission rates and lower precipitation at Fresno, the 4km run

277   simulates higher AOD than the 20km run in the cold season (October-November-December and

278   January-February-March; OND and JFM in Fig. 3). Averaged over a broad area encompassing

279   Fresno and Bakersfield, the most polluted region in the SJV (red box in Fig. 1a), the AOD is 0.090

280   in the 4km and 0.073 in the 20km, a 23% difference. Compared to the MISR observations, the

281   4km simulation reproduces the spatial distribution and magnitude of AOD in the cold season.

282   However, the AOD difference between the 20km and 4km runs is small in the warm season (April-

283   May-June and July-August-September; AMJ and JAS in Fig. 3), and both runs underestimate AOD

284   by ~50% with respect to the MISR observations.

285   Comparing the point values at Fresno in the 4km and 20km simulations (Fig. 4a), we find

286   similar results: the 4km AOD is closer to the AERONET measurements and is about 23% higher

287   than that in the 20km run during the cold season, while both runs are biased low in AOD during

288   the warm season. The different model sensitivities to horizontal resolution between the cold and

289   warm seasons suggest that the dominant aerosol sources may be different for the two seasons. We

290   will elaborate upon the aerosol composition in the following section. MISR and AERONET

291   observations display weak seasonal AOD variation in the SJV and at Fresno, respectively, which

292   is not well represented in the 20km and 4km simulations (Fig. 3 and 4a).

293   Aside from AOD, significant seasonal variability of AE (Fig. 4b) is shown at Fresno. AE

294   exhibits a maximum about 1.50 in January and a minimum of 0.98 in April, suggesting relatively

295   small particles in the winter and large particles in the spring. A relatively large AE value of 1.40

296   (corresponding to small particles) is observed in July, possibly related to the wild fires in late July

297   in the SJV. WRF-Chem captures the seasonal variability of the AE well, with a correlation of 0.90

298   in both the 20km and 4km simulations. The magnitude of AE is also approximately simulated in

299   the cold season, with a mean of 1.15 (1.20) in the 20km (4km) runs compared to 1.33 in the

300   observation. However, the simulated AE is underestimated by ~30% in the warm season,

301   indicating that the simulated particle size is biased high during this period.

302   Significant seasonal variability of $PM_{2.5}$ is observed in the SJV urban areas (Fig. 5a and

303   Supplementary Fig. 4a and 5a). $PM_{2.5}$ at Fresno peaks in January (26.18 µg m^{-3}) and reaches a

304   minimum of 7.03 µg m^{-3} in June, with an annual nonattainment value of 12.64 µg m^{-3} (Fig. 5a).

305   Both the 20km and 4km runs approximately capture the observed seasonal variability of $PM_{2.5}$,

306   with a correlation around 0.90 (Table 2). In the cold season, the 4km simulation overestimates

307   $PM_{2.5}$ by 27% while the 20km simulation exhibits a low bias of 19% compared with IMPROVE

308   observations at Fresno (Table 3). The 4km simulation of PM_{10} is in good agreement with

309   IMPROVE in the winter (December, January and February), but has significant low biases of

310   between 30% and 85% in other months (Fig. 5b). The 20km simulation underestimates PM_{10}

311   throughout WY2013.

312   $PM_{2.5}$ is a mixture of nitrate (NO_3), ammonia (NH_4), OM, EC, sulfate (SO_4), dust and other

313   aerosols. High concentrations of $PM_{2.5}$ are primarily the result of NO_3 at Fresno (Fig. 5c). Both

314   simulations produce the seasonal variability of NO_3 with a correlation of 0.94, but high bias of

315   17% (75%) is found in the 20km (4km) simulations during the cold season. As one precursor of

316   NO_3, NO_2 is underestimated by 43% in the 20km run (Fig. 6a). The overestimation in NO_3 and

317   underestimation in NO_2 suggest that the precursor emissions may not the reason for the high biases

318   in NO_3. NH_4 shows a similar performance to NO_3, with an overestimation by 38% (111%) in the

319   20km (4km) runs during the cold seasons (Fig. 5d). As shown later in section 4.3, both NO_3 and

320   NH_4 simulations are quite sensitive to the PBL scheme applied.

321   OM, the second largest contributing species to cold season $PM_{2.5}$ in the SJV (Table 3), is

322   significantly underestimated by 82% in the 20km simulation (Fig. 5f). The 4km simulation

323   produces higher OM, but it is still lower than the IMPROVE observations by 63%. The

324   underestimation of OM is expected, because SOA processes are not included in our model

325   infrastructure. Fast et al. (2014) used the simplified two-product volatility basis set

326   parameterization to simulate equilibrium SOA partitioning in WRF-Chem although SOA was still

327   underestimated in their simulation. It remains ongoing research how to correctly represent SOA

328   processes in regional climate models.

329   Both the 20km and 4km simulations reproduce the seasonal variability of EC, with a

330   correlation of 0.98 between the modeled and observed time series (Table 2). The 20km simulation

331   underestimates EC by 52% (16%) in the cold (warm) season (Fig. 5e and Table 3). The 4km

332   simulated EC (1.12 μg m^{-3}) exhibits good agreement with IMPROVE (1.08 μg m^{-3}) in the cold

333   season, but overestimates EC by 53% in the warm season.

334   The seasonal variability of SO_4 at Fresno is very different from other $PM_{2.5}$ species. It peaks

335   in May at 1.35 μg m^{-3} and reaches the minimum of 0.67 μg m^{-3} in August (Fig. 5g). The 20km

336   simulated SO_4 exhibits good correlation of 0.63 with the observation (Table 2), but is biased low

337   by 28% to 63% throughout WY2013 (Fig. 5g). Although the observed SO_2, the precursor of SO_4,

338   has approximately similar seasonal variation to the observed SO_4 (Fig. 6b), the 20km simulated

339   seasonal variability of SO_2 resembles other anthropogenic emissions, with high values in the cold

340   season and low values in the warm season, out of phase with the simulated SO_4 and the observed

341   SO$_2$. The 4km simulation produces higher SO$_4$ than the 20km run, resulting in better agreement

342   with the observation (0.82 μg m^{-3} vs. 0.87 μg m^{-3}) during the cold season (Fig. 5g and Table 3).

343   However, the 4km run produces an increase of SO$_4$ by only 13% comparing to the 20km run in

344   the warm season, resulting in a correlation of -0.16 between the 4km simulation and the

345   observation.

346   To explore the possible cause for the underestimation of SO$_4$ and SO$_2$ in the warm season

347   in both the 20km and 4km simulations, we conduct a sensitivity experiment with different chemical

348   boundary conditions from the baseline runs (20km_BC1 in the supplementary). We find that SO$_4$

349   in the SJV is partly contributed to by marine intrusions (the different chemical boundary conditions

350   between 20km_BC1 and 20km_D2) throughout the year (supplementary Fig. 2g), as pointed out

351   by Fast et al. (2014). Including the marine intrusions, the 20km_BC1 simulated SO$_4$ tracks the

352   observation at a correlation of 0.78. Doubled chemical boundary conditions in the 20km simulation

353   results in 41% increase in SO$_4$ at Fresno, with a stronger increase in the warm season. Compared

354   to the observed SO$_4$ of 1.04 μg m^{-3} in the warm season, the simulated SO$_4$ of 0.79 μg m^{-3} in the

355   20km_BC1 run is closer to the observation than that simulated in the 20km_D2 run (0.53 μg m^{-3}).

356   The relative contributions of local emissions and remote transports (as well as other emission

357   sources, such as wild fires) to SO$_4$ concentrations in different seasons of the SJV require further

358   investigation.

359   Overall, the 4km simulation produces higher AOD and surface PM than the 20km

360   simulation in urban areas of the SJV, especially during the cold season, resulting in better

361   agreement with satellite and surface observations than the 20km simulation. Both the 20km and

362   4km simulations approximately capture the seasonal variability of PM$_{2.5}$ and most of its speciation.

363   However, significant low biases of AOD and PM$_{10}$ are found during the warm season in both

364   simulations. The underestimation also exists in a sensitivity experiment (not shown) with the same

365   model setups except initialized in April, indicating that the identified model biases during the warm

366   season are not caused by potential model drift after a relatively long simulation period. The

367   relatively good performance in simulating $PM_{2.5}$ but not PM_{10} during the warm season suggests

368   that coarse aerosol particle mass (CM; 10 μm ≥ particulate matter with diameter > 2.5 μm), mainly

369   dust in the SJV, is not properly represented in the model. The impact of dust parameterizations is

370   investigated in the 4km_D2 experiment.

371   **4.2 Sensitivity to Dust Scheme**

372   Limited amounts of $PM_{2.5}$_dust (dust with diameter ≤ 2.5 μm) are observed in the SJV cold

373   season, with a minimum of 0.37 μg m^{-3} in December (Fig. 7a). The amount of $PM_{2.5}$_dust increases

374   in the warm season, with a peak of 3.86 μg m^{-3} in September. The 4km simulation produces

375   comparable $PM_{2.5}$_dust relative to IMPROVE in the winter, but almost no dust in other months

376   (Fig. 7 and upper panel in Fig. 8). On the other hand, the dust emission rate in the 4km_D2 run is

377   significantly higher than the 4km run. We have found that the source function, S, for potential

378   wind erosion in the SJV is set to zero in the 1°x1° GOCART dataset used for the 4km simulation

379   (Fig. 9). An updated source function, S, at higher resolution is needed for the GOCART dust

380   scheme to correctly represent dust emissions in the SJV.

381   The 4km_D2 simulation reproduces the amount of $PM_{2.5}$_dust in OND (Fig. 7a). However,

382   it overestimates $PM_{2.5}$_dust by up to a factor of 3 in the warm season, resulting in an overestimation

383   of $PM_{2.5}$ by 52% (Fig. 7b and Table 3). $PM_{2.5}$_dust is not sensitive to long-range transport (from

384   chemical boundary conditions in the model simulation; Supplementary Fig. 2h). Both the 4km and

385   4km_D2 simulations capture the seasonal variability of $PM_{2.5}$, but not that of PM_{10} (Fig. 7c). The

386   magnitude of PM_{10} in the 4km_D2 run is larger than the 4km simulation. PM_{10} in the 4km_D2 run

387   is overestimated in April-May-June (AMJ) but underestimated in July-August-September (JAS),

388   leading to a comparable season mean of 38.12 μg m^{-3} with IMPROVE observed 34.82 μg m^{-3}. The

389   overestimation of AMJ PM$_{10}$ and PM$_{2.5}$_dust in the 4km_D2 run is likely associated with the high

390   bias in the simulated wind speed (Fig. 2b).

391   On the relative contribution of different aerosol species, IMPROVE observations at Fresno

392   show that NO$_3$ is the primary contributor (32.3%) to PM$_{2.5}$ while only 5.3% of PM$_{2.5}$ is dust in the

393   cold season (panel 1 of Fig. 10). Both the 4km and 4km_D2 runs roughly reproduce the relative

394   contributions to PM$_{2.5}$ in the cold season, with an overestimation of NO$_3$ and NH$_4$ and an

395   underestimation of OM, consistent with the time series in Fig. 5. Relative contributions of dust to

396   PM$_{2.5}$ are better simulated in the 4km_D2 run (7.3%) than the 4km one (<1.0%). IMPROVE shows

397   that 46.6% of PM$_{10}$ is CM in the cold season (panel 2 of Fig. 10). Both the 4km (6.3%) and

398   4km_D2 (20.6%) runs underestimate the contribution of CM to PM$_{10}$, mainly in October and

399   November. In the warm season, dust (24.6%) becomes the primary contributor to PM$_{2.5}$ while the

400   contribution from NO$_3$ decreases to 9.9% in IMPROVE observations (panel 3 of Fig. 10). Almost

401   no PM$_{2.5}$_dust is simulated in the 4km run while too much PM$_{2.5}$_dust is produced in the 4km_D2

402   (50.5%) run during the warm season. The relative contribution of CM to PM$_{10}$ is too small (27.6%)

403   in the 4km run, while the 4km_D2 run reflects an better relative contribution of 66.3% as compared

404   to an IMPROVE observed 75.8% (panel 4 of Fig. 10).

405   AOD simulations are improved in the 4km_D2 experiment (Fig. 11), with better agreement

406   found from MISR (Fig. 3) in AMJ. AOD (0.114) in the 4km_D2 run is comparable to observations

407   (0.131) in AMJ, but still underestimated by 53% in JAS. Consistent with AOD, the vertical

408   distribution of aerosol extinction is reasonably simulated during the cold season in the WRF-Chem

409   simulations, while large discrepancies are found in the warm season (Fig. 12). As observed by

410   CALIOP at 532 nm, aerosols are mainly confined below 1 km above the surface in the cold season.

411   Model simulations roughly capture the vertical distribution of aerosol extinction observed by

412   CALIOP, with low biases in the boundary layer and high biases in the free atmosphere. Similar

413   discrepancy between the model simulations and CALIOP is shown in other studies (Wu et al.,

414   2011a; Hu et al., 2016). The difference between the 4km and 4km_D2 runs is small during the

415   cold season.

416   Dust in the boundary layer is a primary factor contributing to aerosol extinction in the SJV,

417   as illustrated by the differences between the bulk seasonal CALIOP mean profile and those

418   excluding the contributions of the dust and polluted dust (CALIOP_nodust) profiles (Fig. 12).

419   Simulated aerosol extinction falls between the two in all seasons, suggesting that dust is the

420   primary factor contributing to the model biases in aerosol extinction. Although a small portion of

421     $PM_{2.5}$ is dust in the cold season, it contributes to about 50% of total aerosol extinction (Fig. 12a

422   and 12b). A predominant portion of aerosol extinction in the boundary layer is contributed by dust

423   in the warm season (Fig. 12c and 12d). There, the 4km_D2 simulation produces higher aerosol

424   extinction in the boundary layer than the 4km simulation, although it is still lower than CALIOP.

425   The simulated aerosol extinction in the free troposphere above the boundary layer is close to or

426   larger than CALIOP, suggesting that aerosols transported from remote areas through chemical

427   boundary conditions (e.g., the differences between the 20km_BC1 and 20km_D2 runs in

428   Supplementary Fig. 3) may not be the major factor contributing to the underestimation of dust in

429   the boundary layer in the SJV.

430   Overall, the poor simulations of dust in the boundary layer play a dominant role in the low

431   bias of aerosols during the warm season. Both the GOCART and DUSTRAN dust emission

432   schemes used in this study have difficulties in reproducing dust emissions in the SJV, with an

433   underestimation in GOCART and an overestimation in DUSTRAN (Fig. 7). Improvement on the

434   dust emission schemes is needed for capturing the seasonal variability of aerosols in the SJV.

4.3 The Role of Meteorology

436   The WRF-Chem simulations approximately reproduce the seasonal variations of

437   meteorological variables near the surface (correlations > 0.80), including temperature, RH, wind

438   speed and precipitation (Supplementary Fig. 6 and Supplementary Table 1). All of the model

439   simulations exhibit warm and dry biases near surface and in the boundary layer, with cold and wet

440   biases in the free atmosphere (Supplementary Fig. 6-8 and Supplementary Table 2). The dry bias

441   in the 4km_D2 run is about 10% near the surface throughout WY2013. Due to the relative dry

442   environment (RH<50%) in the warm season, the dry bias is likely not responsible for the

443   underestimation of boundary layer aerosol extinctions and column-integrated AOD through

444   hygroscopic effects (Feingold and Morley, 2003). In the cold season, the surface wind speed is

445   underestimated by 0.67 m/s (1.00 m/s) in the 4km_D2 (20km_D2) runs. In the warm season, the

446   4km_D2 run overestimates wind speed by 0.78 m/s, while the 20km_D2 run has an

447   underestimation of 0.16 m/s. These results suggest that wind speed is also not the primary factor

448   contributing to low biases in the boundary layer aerosols. The seasonal variability of precipitation

449   is well captured in the simulations, while the magnitude of precipitation is smaller than the

450   observations during the warm season (Supplementary Table 2). Wet removal processes are thus

451   not likely the primary reason for the aerosol biases in the warm season.

452   In the warm season, more aerosols are observed at higher altitude than during the cold

453   season (Fig. 12). A well-mixed layer of aerosols is observed below 1.5 km in AMJ (Fig. 12c),

454   consistent with the unstable layers below 1.5 km observed by AIRS (Fig. 13c). However, the WRF-

455   Chem model simulates neutral (or weakly stable) layers below 1.5 km (Fig. 13c), which may lead

456   to a failure in capturing the well-mixed layer of aerosols (Fig. 12c). Although the dust emission at

457   the surface is large in the 4km_D2 run, not enough convective vertical mixing is produced in the

458   simulations, plausibly resulting in the low biases found in the boundary layer. Aerosol extinction

459   gradually decreases with height in the simulations. Similar biases of aerosol and instability in the

460   boundary layer are also shown in JAS (Fig. 12d and 13d). Relative static stability in the simulations,

461   which limits convective vertical mixing of aerosols, likely enhances the low bias of column-

462   integrated AOD in JAS (Fig. 11). Although the 4km_D2 experiment produces comparable AOD

463   and surface PM mass in AMJ (Fig. 6 and Fig. 11), the vertical distribution of aerosols is not well

464   represented (Fig. 12). The comparable AOD in the 4km_D2 run results from the low bias in the

465   boundary layer and the high bias in the free atmosphere. In JAS (Fig. 12d), comparable aerosol

466   extinction to CALIOP is simulated in the free atmosphere, suggesting that the low bias in AOD is

467   not due to the halved chemical boundary conditions from MOZART-4. Albeit some discrepancies

468   in the magnitude of atmospheric stability, all of the simulations capture the stable environment in

469   the cold season (Fig. 13a and 13b), consistent with relatively good performance of aerosol

470   simulations in the cold season.

471   As biases in the model simulations are found mainly within the boundary layer, a sensitivity

472   experiment is conducted at 20 km resolution using the ACM2 PBL scheme (20km_P7). Although

473   the changes in the meteorological variables (Supplementary Fig. 6-8) and atmospheric static

474   stability (Fig. 13) are rather small, the simulated surface NO_3 and NH_4 in the 20km_P7 run

475   decrease by 50% compared to the 20km_D2 run (Fig. 14c, 14d and Table 3). Considering that

476   more NO_3 and NH_4 are simulated at 4 km resolution than at 20 km resolution as shown in section

477   4.1, the use of the ACM2 PBL scheme at 4 km simulation would largely resolve the high biases

478   of NO_3 and NH_4 in the 4km_D2 simulation. The decrease of NO_3 and NH_4 at the surface is because

479   more aerosols are transported to the layers above 0.5 km (Fig. 15a and 15b), resulting from

480   different convective vertical mixing in the PBL schemes. However, $PM_{2.5}$_dust is significantly

481   overestimated by a factor of 4 in the 20km_P7 simulation (Fig. 14h), leading to a small decrease

482   of $PM_{2.5}$ by only 8% compared with the 20km_D2 run in the cold season. In the warm season,

483    $PM_{2.5}$_dust in the 20km_P7 run is overestimated by a factor of 5, causing an overestimation of

484    $PM_{2.5}$ and PM_{10} (Fig. 14a and 14b). Aerosol extinctions in the boundary layer increase in the warm

485   season (Fig. 15c and 15d), possibly related to overestimation of dust emissions and more

486   conducive convective vertical transport in the PBL scheme.

487   In summary, the WRF-Chem model captures the seasonal variations of meteorological

488   variables (temperature, RH, wind speed and precipitation), despite some deviations in magnitude.

489   The low biases in aerosol optical properties of the warm season likely do not originate from

490   hygroscopic effects, wet removal processes or dust emissions associated with the wind speed bias.

491   The model simulates a stable environment in the warm season, which is opposite to the observed

492   unstable environment. The simulated stable environment may be most likely responsible for low

493   biases in the aerosol extinction in the boundary layer and the column-integrated AOD in the warm

494   season. Switching to the ACM2 PBL scheme leads to improved vertical mixing in the boundary

495   layer, thus an improvement in the simulations of NO_3 and NH_4 in the cold season. However, dust

496   emissions are significantly overestimated with the ACM2 PBL scheme, which contributes partly

497   to the better simulation of aerosol extinction in the boundary layer and AOD in the column. These

498   results highlight that improving the simulation of boundary layer structure and processes are

499   critical for capturing the vertical profiles of aerosol extinction.

500   **4.4 Results in Rural Areas**

501   In general, low values of PM concentration are observed in the rural areas, Pinnacles and

502   Kaiser (Fig. 16 and 17). The rural areas share some similar model performance to the urban areas,

503   such as the overestimation of NO_3, reasonable simulation of EC, good representation of SO_4 in the

504   cold season and underestimation of SO_4 in the warm season. However, the results are not sensitive

505   to model resolution. It suggests that high resolution is particularly important for heavily polluted

506   areas due to the inhomogeneity of emission sources, but less important for relatively lightly

507   polluted areas.

508   In late July/early August, MODIS (Moderate Resolution Imaging Spectroradiometer) fire

509   data (not shown) showed active wild fires close to Kaiser, which resulted in high concentration of

510   aerosols locally (Fig. 17). Our model simulations with monthly-varying fire emissions fail to

511   reproduce these fire events. Previous studies (e.g., Grell et al., 2011; Wu et al. 2011a; Archer-

512   Nicholls et al., 2015) demonstrated that the WRF-Chem model can capture aerosols distributions

513   from wild fires based on fire locations from satellite observations. Campbell et al. (2016) further

514   described the difficulties in constraining total aerosol mass from operational satellite fire

515   observations and the time needed by the model for diffusion within the near-surface layers to

516   render both reasonable AOD and vertical profiles of aerosol extinction. For operational application

517   of the WRF-Chem model in MAIA retrievals, the observations of daily fire events need to be more

518   appropriately considered.

519 **5. Summary**

520   The WRF-Chem (Weather Research and Forecasting model with Chemistry) model is

521   employed to simulate the seasonal variability of aerosols in WY2013 (water year 2013) in the SJV

522   (San Joaquin Valley). Model simulations are evaluated using satellite and in-situ observations. In

523   general, the model simulations conducted at 4 km resolution reproduce the spatial and temporal

524   variations of regional aerosols in the cold season, when aerosols are mainly contributed to by

525   anthropogenic emissions in the SJV. The magnitude of simulated aerosols in the cold season

526   however, especially in relatively dense urban areas, is sensitive to model horizontal resolution.

527   The 4km simulation has comparable magnitude to available observations, while the 20km

528   simulation underestimates aerosols. Differences in aerosol simulation fidelity as a function of

529   variable resolutions are mainly due to the difference in aerosol emissions and simulated

530   precipitation. Emissions at higher resolution can better resolve the inhomogeneity of

531   anthropogenic emissions in the SJV than at lower resolution. The sensitivity to horizontal

532   resolution is small in rural areas and during warm season, where/when the relative contribution of

533   anthropogenic emissions is small.

534   Previous studies in the SJV are mainly focused on $PM_{2.5}$ (particulate matter with diameter

535   ≤ 2.5 μm) and during cold season (e.g. Chow et al., 2006; Herner et al., 2006; Pun et al., 2009;

536   Ying and Kleeman, 2009; Zhang et al., 2010; Chen et al., 2014; Hasheminassab et al., 2014; Kelly

537   et al., 2014; Baker et al., 2015; Brown et al., 2016). CALIOP (Cloud-Aerosol Lidar with

538   Orthogonal Polarization) and IMPROVE (Interagency Monitoring of Protected Visual

539   Environments) observations show that dust is a primary contributor to the aerosols in the SJV,

540   especially in the warm season. Dust contributes 24.6% to $PM_{2.5}$ while more than 75.8% to PM_{10} in

541   the warm season. For all seasons, the major component of aerosol extinction in the boundary layer

542   is dust as observed by CALIOP, consistent with Kassianov et al. (2012). For a complete

543   understanding of aerosol impacts on air quality, weather and climate, the full spectrum of aerosols

544   should be considered during all seasons.

545   All the model simulations conducted fail to capture aerosol vertical distribution and

546   variability in the SJV warm season, largely due to the misrepresentation of dust emissions, static

547 stability and vertical mixing in the boundary layer. The GOCART (Goddard Global Ozone

548 Chemistry Aerosol Radiation and Transport) dust emission scheme significantly underestimates

549 dust due to the non-active source function, S, for potential wind erosion used in this study while

550 the DUSTRAN (DUST TRANsport model) scheme may overestimate dust emission in the SJV.

551 Along with the bias in dust emissions, our simulations produce a relatively stable boundary layer

552 in the warm season, in contrast with observations suggesting a more unstable environment, leading

553 to a weak vertical mixing of aerosols in the boundary layer. Improved dust emission and better

554 simulations of the boundary layer properties are needed for accurate simulation of aerosols in the

555 SJV warm season.

556 Other biases are also identified in the model simulations. NO_3 and NH_4 in the cold season

557 are overestimated in the model, but the results are sensitive to the choice of the PBL (planetary

558 boundary layer) scheme. The SOA (secondary organic aerosol) processes contribute to the

559 underestimation of OM (organic matter) in this study. The underestimation of sulfate in the warm

560 season may be caused by the misrepresentation of emissions and the chemical boundary conditions

561 related to marine intrusions. Aerosols from wild fires are not captured in the simulations with

562 monthly updated fire data. Further investigations are needed to improve model simulations in the

563 SJV for both scientific and operational applications.

Acknowledgements

565 This study was carried out at the Jet Propulsion Laboratory, California Institute of

566 Technology, under a contract with the National Aeronautics and Space Administration. The

567 authors thank the funding support from the NASA ACMAP program and JPL PDF program. This

568 work is partially sponsored by California Energy Commission under grant #EPC-14-064. Author

569 JRC acknowledges the support of the NASA ACCDAM program and its manager Hal Maring.

570 The authors thank the three anonymous reviewers for their helpful comments.

571 **References**

572 Archer-Nicholls, S., Lowe, D., Darbyshire, E., Morgan, W. T., Bela, M. M., Pereira, G., Trembath,

573   J., Kaiser, J. W., Longo, K. M., Freitas, S. R., Coe, H., and McFiggans, G.: Characterising

574   Brazilian biomass burning emissions using WRF-Chem with MOSAIC sectional aerosol,

575   Geosci. Model Dev., 8, 549-577, doi:10.5194/gmd-8-549-2015, 2015.

576 Ångström, A.: On the atmospheric transmission of Sun radiation and on dust in the air, Geogr.

577   Ann., 11, 156–166, 1929.

578 Baker, K. R., Carlton, A. G., Kleindienst, T. E., Offenberg, J. H., Beaver, M. R., Gentner, D. R.,

579   Goldstein, A. H., Hayes, P. L., Jimenez, J. L., Gilman, J. B., de Gouw, J. A., Woody, M. C.,

580   Pye, H. O. T., Kelly, J. T., Lewandowski, M., Jaoui, M., Stevens, P. S., Brune, W. H., Lin, Y.-

581   H., Rubitschun, C. L., and Surratt, J. D.: Gas and aerosol carbon in California: comparison of

582   measurements and model predictions in Pasadena and Bakersfield, Atmos. Chem. Phys., 15,

583   5243-5258, doi:10.5194/acp-15-5243-2015, 2015.

584 Barnard, J. C., Fast, J. D., Paredes-Miranda, G., Arnott, W. P., and Laskin, A.: Technical Note:

585   Evaluation of the WRF-Chem "Aerosol Chemical to Aerosol Optical Properties" Module using

586   data from the MILAGRO campaign, Atmos. Chem. Phys., 10, 7325–7340, doi:10.5194/acp-

587   10-7325-2010, 2010.

588 Brown, S. G., Hyslop, N. P., Roberts, P. T., McCarthy, M. C., and Lurmann, F. W.: Wintertime

589   vertical variations in particulate matter (PM) and precursor concentrations in the San Joaquin

590   Valley during the California Regional Coarse PM/Fine PM Air Quality Study, J. Air Waste

591   Manage., 56, 1267–1277, 2006.

592 Campbell, J. R., Tackett, J. L., Reid, J. S., Zhang, J., Curtis, C. A., Hyer, E. J., Sessions, W. R.,

593   Westphal, D. L., Prospero, J. M., Welton, E. J., Omar, A. H., Vaughan, M. A., and Winker, D.

594   M.: Evaluating nighttime CALIOP 0.532 μm aerosol optical depth and extinction coefficient

595   retrievals, Atmos. Meas. Tech., 5, 2143-2160, doi:10.5194/amtd-5-2143-2012, 2012.

596 Campbell., J. R., Ge, C., Wang, J., Welton, E. J., Bucholtz, A., Hyer, E. J., Reid, E. A., Chew, B.
597 N., Liew, S.-C., Salinas, S. V., Lolli, S., Kaku, K. C., Lynch, P., Mahmud, M., Mohamad, M.,
598 and Holben, B. N.: Applying Advanced Ground-Based Remote Sensing in the Southeast Asian
599 Maritime Continent to Characterize Regional Proficiencies in Smoke Transport Modeling, J.
600 Appl. Meteorol. Climatol., 55, 3-22, doi: http://dx.doi.org/10.1175/JAMC-D-15-0083.1, 2016.

601 Chapman, E. G., Gustafson Jr., W. I., Easter, R. C., Barnard, J. C., Ghan, S. J., Pekour, M. S., and
602 Fast, J. D.: Coupling aerosolcloud-radiative processes in the WRF-Chem model: Investigating
603 the radiative impact of elevated point sources, Atmos. Chem. Phys., 9, 945–964,
604 doi:10.5194/acp-9-945-2009, 2009.

605 Chen, J., Lu, J., Avise, J. C., DaMassa, J. A., Kleeman, M. J., and Kaduwela, A. P.: Seasonal
606 modeling of PM2.5 in California's San Joaquin Valley, Atmos. Environ., 92, 182–190, 2014.

607 Chew, B. N., J. R. Campbell, J. S. Reid, D. M. Giles, E. J. Welton, S. V. Salinas and S. C. Liew:
608 Tropical cirrus cloud contamination in sun photometer data, Atmos. Env., 45, 6724-6731,
609 doi:10.1016/j.atmosenv.2011.08.017, 2011.

610 Chow, J. C., Chen, L. W. A., Watson, J. G., Lowenthal, D. H., Magliano, K. A., Turkiewicz, K.,
611 Lehrman, D. E.: PM2.5 chemical composition and spatiotemporal variability during the
612 California regional PM10/PM2.5 air quality study (CRPAQS), J. Geophys. Res.-Atmos., 111,
613 D10S04, doi:10.1029/2005JD006457, 2006.

614 Dee, D. P., Uppala, S. M., Simmons, A. J., Berrisford, P., Poli, P, Kobayashi, S., Andrae, U.,
615 Balmaseda, M. A., Balsamo, G., Bauer, P., Bechtold, P., Beljaars, A. C. M., van de Berg, L.,
616 Bidlot, J., Bormann, N., Delsol, C., Dragani, R., Fuentes, M., Geer, A. J., Haimberger, L.,
617 Healy, S. B., Hersbach, H., Hólm, E. V., Isaksen, L., Kallberg, P., Köhler, M., Matricardi, M.,
618 McNally, A. P., Monge-Sanz, B. M., Morcrette, J.-J., Park, B.-K., Peubey, C., de Rosnay, P.,
619 Tavolato, C., Thépaut, J.-N., and Vitart, F.: The ERA-Interim reanalysis: configuration and
620 performance of the data assimilation system, Q. J. R. Meteorol. Soc., 137, 553–597, 2011.

621 Diner, D. J., Beckert, J. C., Reilly, T. H., Bruegge, C. J., Conel, J. E., Kahn, R. A., Martonchik, J.
622 V., Ackerman, T. P., Davies, R., Gerstl, S. A. W., Gordon, H. R., Muller, J. P., Myneni, R. B.,
623 Sellers, P. J., Pinty, B., and Verstraete, M. M.: Multi-angle Imaging SpectroRadiometer

624   (MISR) Instrument Description and Experiment Overview, IEEE T. Geosci. Remote, 36,
625   1072–1087, 1998.

626 Divakarla, M. G., Barnet, C. D., Goldberg, M. D., McMillin, L. M., Maddy, E., Wolf, W., Zhou,
627   L., and Liu, X.: Validation of Atmospheric Infrared Sounder temperature and water vapor
628   retrievals with matched radiosonde measurements and forecasts, J. Geophys. Res., 111,
629   D09S15, doi:10.1029/2005JD006116, 2006.

630 Eck, T. F., Holben, B. N., Reid, J. S., Dubovik, O., Smirnov, A., O'Neill, N. T., Slutsker, I., and
631   Kinn, S.: Wavelength dependence of the optical depth of biomass burning urban, and desert
632   dust aerosols, J. Geophys. Res., 104, 31333–31349, 1999.

633 Emmons, L. K., Walters, S., Hess, P. G., Lamarque, J.-F., Pfister, G. G., Fillmore, D., Granier, C.,
634   Guenther, A., Kinnison, D., Laepple, T., Orlando, J., Tie, X., Tyndall, G., Wiedinmyer, C.,
635   Baughcum, S. L., and Kloster, S.: Description and evaluation of the Model for Ozone and
636   Related chemical Tracers, version 4 (MOZART-4), Geosci. Model Dev., 3, 43–67, doi:
637   10.5194/gmd-3-43-2010, 2010.

638 Fast, J. D., Gustafson Jr., W. I., Easter, R. C., Zaveri, R. A., Barnard, J. C., Chapman, E. G., Grell,
639   G. A. and Peckham, S. E.: Evolution of ozone, particulates, and aerosol direct radiative forcing
640   in the vicinity of Houston using a fully coupled meteorology-chemistry-aerosol model, J.
641   Geophys. Res., 111, D21305, doi:10.1029/2005JD006721, 2006.

642 Fast, J. D., Gustafson Jr., W. I., Berg, L. K., Shaw, W. J., Pekour, M., Shrivastava, M., Barnard, J.
643   C., Ferrare, R. A., Hostetler, C. A., Hair, J. A., Erickson, M., Jobson, B. T., Flowers, B., Dubey,
644   M. K., Springston, S., Pierce, R. B., Dolislager, L., Pederson, J., and Zaveri, R. A.: Transport
645   and mixing patterns over Central California during the carbonaceous aerosol and radiative
646   effects study (CARES), Atmos. Chem. Phys., 12, 1759-1783, doi:10.5194/acp-12-1759-2012,
647   2012.

648 Fast, J. D., Allan, J., Bahreini, R., Craven, J., Emmons, L., Ferrare, R., Hayes, P. L., Hodzic, A.,
649   Holloway, J., Hostetler, C., Jimenez, J. L., Jonsson, H., Liu, S., Liu, Y., Metcalf, A.,
650   Middlebrook, A., Nowak, J., Pekour, M., Perring, A., Russell, L., Sedlacek, A., Seinfeld, J.,
651   Setyan, A., Shilling, J., Shrivastava, M., Springston, S., Song, C., Subramanian, R., Taylor, J.
652   W., Vinoj, V., Yang, Q., Zaveri, R. A., and Zhang, Q.: Modeling regional aerosol and aerosol

precursor variability over California and its sensitivity to emissions and long-range transport during the 2010 CalNex and CARES campaigns, Atmos. Chem. Phys., 14, 10013-10060, doi:10.5194/acp-14-10013-2014, 2014.

Feingold, G., and Morley, B.: Aerosol hygroscopic properties as measured by lidar and comparison with in situ measurements, J. Geophys. Res., 108(D11), 4327, doi:10.1029/2002JD002842, 2003.

Flanner, M. G., and Zender, C. S.: Snowpack radiative heating: Influence on Tibetan Plateau climate, Geophys. Res. Lett., 32, L06501, doi:10.1029/2004GL022076, 2005.

Flanner, M. G., and Zender, C. S.: Linking snowpack microphysics and albedo evolution, J. Geophys. Res., 111, D12208, doi:10.1029/2005JD006834, 2006.

Fountoukis, C., Koraj, D., Denier van der Gon, H. A. C., Charalampidis, P. E., Pilinis, C., and Pandis, S. N.: Impact of grid resolution on the predicted fine PM by a regional 3-D chemical transport model, Atmos. Environ., 68, 24–32, 2013.

Freitas, S. R., Longo, K. M., Alonso, M. F., Pirre, M., Marecal, V., Grell, G., Stockler, R., Mello, R. F., and Sánchez Gácita, M.: PREP-CHEM-SRC – 1.0: a preprocessor of trace gas and aerosol emission fields for regional and global atmospheric chemistry models, Geosci. Model Dev., 4, 419-433, doi:10.5194/gmd-4-419-2011, 2011.

Ghan, S., Laulainen, N., Easter, R., Wagener, R., Nemesure, S., Chapman, E., Zhang, Y., and Leung, R.: Evaluation of aerosol direct radiative forcing in MIRAGE, J. Geophys. Res., 106(D6), 5295–5316, doi:10.1029/2000JD900502, 2001.

Ginoux, P., Chin, M., Tegen, I., Prospero, J. M., Holben, B., Dubovik, O., and Lin, S.: Sources and distributions of dust aerosols simulated with the GOCART model, J. Geophys. Res., 106, 20225–20273, 2001.

Gong, S. L.: A parameterization of sea-salt aerosol source function for sub- and super-micron particles, Global Biogeochem. Cy., 17, 1097, doi:10.1029/2003GB002079, 2003.

Grell, G. and Devenyi, D.: A generalized approach to parameterizing convection combining ensemble and data assimilation techniques, Geophys. Res. Lett., 29(14), doi:10.1029/2002GL015311, 2002.

681 Grell, G., Peckham, S., Schmitz, R., et al.: Fully coupled "online" chemistry within the WRF
682   model, Atmos. Environ., 39(37), 6957–6975, 2005.

683 Grell, G., Freitas, S. R., Stuefer, M., and Fast, J.: Inclusion of biomass burning in WRF-Chem:
684   impact of wildfires on weather forecasts, Atmos. Chem. Phys., 11, 5289-5303,
685   doi:10.5194/acp-11-5289-2011, 2011.

686 Guenther, A., Karl, T., Harley, P., Wiedinmyer, C., Palmer, P. I., and Geron, C.: Estimates of
687   global terrestrial isoprene emissions using MEGAN (Model of Emissions of Gases and
688   Aerosols from Nature), Atmos. Chem. Phys., 6, 3181–3210, doi: 10.5194/acp-6-3181-2006,
689   2006.

690 Hand, J., Copeland, S. A., Day, D. E., Dillner, A. M., Indresand, H., Malm, W. C., McDade, C.
691   E., Moore Jr., C. T., Pitchford, M. L., Schichtel, B. A., and Watson, J. G.: Spatial and seasonal
692   patterns and temporal variability of haze and its constituents in the United States: Report V,
693   June 2011, available at: http://vista.cira.colostate.edu/Improve/spatial-and-seasonal-patterns-
694   and-temporal-variability-of-haze-and-its-constituents-in-the-united-states-report-v-june-
695   2011/, 2011.

696 Hasheminassab, S., Daher, N., Saffari, A., Wang, D., Ostro, B. D., and Sioutas, C.: Spatial and
697   temporal variability of sources of ambient fine particulate matter ($PM_{2.5}$) in California, Atmos.
698   Chem. Phys., 14, 12085-12097, doi:10.5194/acp-14-12085-2014, 2014.

699 Herner, J. D., Ying, Q., Aw, J., Gao, O., Chang, D. P. Y., and Kleeman, M.: Dominant mechanisms
700   that shape the airborne particle size and composition in central California, Aerosol Sci.
701   Technol., 40, 827–844, 2006.

702 Holben, B. N., Eck, T. F., Slutsker, I., Tanre ì, D., Buis, J. P., Setzer, A., Vermote, E., Reagan, J.
703   A., Kaufman, Y. J., Nakajima, T., Lavenu, F., Jankowiak, I., and Smirnov, A.: AERONET –
704   A Federated Instrument Network and Data Archive for Aerosol Characterization, Remote
705   Sens. Environ., 66, 1–16, 1998.

706 Holben, B. N., Tanr, D., Smirnov, A., Eck, T. F., Slutsker, I., Abuhassan, N., Newcomb, W. W.,
707   Schafer, J. S., Chatenet, B., Lavenu, F., Kaufman, Y. J., Castle, J. V., Setzer, A., Markham,
708   B., Clark, D., Frouin, R., Halthore, R., Karneli, A., O'Neill, N. T., Pietras, C., Pinker, R. T.,

709   Voss, K., and Zibordi, G.: An emerging ground-based aerosol climatology: Aerosol optical
710   depth from AERONET, J. Geophys. Res., 106, 12067–12097, 2001.

711   Hong, S., Noh, Y., and Dudhia, J.: A new vertical diffusion package with an explicit treatment of
712   entrainment processes, Mon. Weather Rev., 134, 2318–2341, 2006.

713   Hu, Z., Zhao, C., Huang, J., Leung, L. R., Qian, Y., Yu, H., Huang, L., and Kalashnikova, O. V.:
714   Trans-Pacific transport and evolution of aerosols: evaluation of quasi-global WRF-Chem
715   simulation with multiple observations, Geosci. Model Dev., 9, 1725-1746, doi:10.5194/gmd-
716   9-1725-2016, 2016.

717   Iacono, M. J., Delamere, J. S., Mlawer, E. J., Shephard, M. W., Clough, S. A., and Collins, W. D.:
718   Radiative forcing by long-lived greenhouse gases: calculations with the AER radiative transfer
719   models, J. Geophys. Res., 113, D13103, doi:10.1029/2008JD009944, 2008.

720   Jaeglé, L., Quinn, P. K., Bates, T. S., Alexander, B., and Lin, J.-T.: Global distribution of sea salt
721   aerosols: new constraints from in situ and remote sensing observations, Atmos. Chem. Phys.,
722   11, 3137–3157, doi:10.5194/acp-11-3137-2011, 2011.

723   Kahn, R. A., Gaitley, B. J., Garay, M. J., Diner, D. J., Eck, T. F., Smirnov, A., and Holben, B. N.:
724   Multiangle Imaging SpectroRadiometer global aerosol product assessment by comparison with
725   the Aerosol Robotic Network, J. Geophys. Res., 115, D23209, doi:10.1029/2010JD014601,
726   2010.

727   Kassianov, E., Pekour, M., and Barnard, J.: Aerosols in central California: Unexpectedly large
728   contribution of coarse mode to aerosol radiative forcing, Geophys. Res. Lett., 39, L20806, doi:
729   10.1029/2012GL053469, 2012.

730   Kelly, J. T., Baker, K. R., Nowak, J. B., Murphy, J. G., Markovic, M. Z., VandenBoer, T. C., Ellis,
731   R. A., Neuman, J. A., Weber, R. J., and Roberts, J. M.: Fine-scale simulation of ammonium
732   and nitrate over the South Coast Air Basin and San Joaquin Valley of California during
733   CalNex-2010, J. Geophys. Res.-Atmos., 119, 3600–3614, 2014.

734   Lawrence, D. M., Oleson, K. W., Flanner, M. G., Thornton, P. E., Swenson, S. C., Lawrence, P.
735   J., Zeng, X., Yang, Z.-L., Levis, S., Sakaguchi, K., Bonan, G. B., and Slater, A. G.:
736   Parameterization improvements and functional and structural advances in version 4 of the

737   Community Land Model, J. Adv. Model. Earth Sys., 3, M03001, doi:
738   10.1029/2011MS000045, 2011.

739   Misenis, C. and Zhang, Y.: An examination of sensitivity of WRF/Chem predictions to physical
740   parameterizations, horizontal grid spacing, and nesting options, Atmos. Res., 97, 315–334,
741   doi:10.1016/j.atmosres.2010.04.005, 2010.

742   Morabito, D., Wu, L., and Slobin, S.: Weather Forecasting for Ka-band Operations: Initial Study
743   Results, IPN PR 42-206, pp. 1-24, August 15, 2016. Available at:
744   http://ipnpr.jpl.nasa.gov/progress_report/42-206/206C.pdf, 2016.

745   Morrison, H., Thompson, G., and Tatarskii, V.: Impact of cloud microphysics on the development
746   of trailing stratiform precipitation in a simulated squall line: comparison of one- and two-
747   moment schemes, Mon. Weather Rev., 137, 991–1007, 2009.

748   Omar, A.H., Winker, D.M., Kittaka, C., Vaughan, M.A., Liu, Z., Hu, Y., Trepte, C.R., Rogers,
749   R.R., Ferrare, R.A., Lee, K.P., Kuehn, R.E., Hostetler, C.A.: The CALIPSO automated aerosol
750   classification and lidar ratio selection algorithm. J. Atmos. Ocean. Technol. 26, 1994–2014,
751   2009.

752   Pleim, J. E.: A combined local and nonlocal closure model for the atmospheric boundary layer.
753   Part I: Model description and testing, J. Appl. Meteorol. Clim., 46, 1383–1395, 2007.

754   Pun, B. K., Balmori, R. T. F., and Seigneur, C.: Modeling wintertime particulate matter formation
755   in central California, Atmos. Environ., 43, 402–409, 2009.

756   Qian, Y., Gustafson Jr., W. I., and Fast, J. D.: An investigation of the sub-grid variability of trace
757   gases and aerosols for global climate modeling, Atmos. Chem. Phys., 10, 6917-6946,
758   doi:10.5194/acp-10-6917-2010, 2010.

759   Randerson, J. T., van der Werf, G. R., Giglio, L., Collatz, G. J., and Kasibhatla, P. S.: Global Fire
760   Emissions Database, Version 2 (GFEDv2.1). Data set. Available on-line [http://daac.ornl.gov/]
761   from Oak Ridge National Laboratory Distributed Active Archive Center, Oak Ridge,
762   Tennessee, U.S.A. doi:10.3334/ORNLDAAC/849, 2007.

763   San Joaquin Valley Air Pollution Control District: 2012 PM2.5 plan. Available from:
764   http://www.valleyair.org/Air_Quality_Plans/PM25Plans2012.htm, 2012.

765 Scarino, A. J., Obland, M. D., Fast, J. D., Burton, S. P., Ferrare, R. A., Hostetler, C. A., Berg, L.
766   K., Lefer, B., Haman, C., Hair, J. W., Rogers, R. R., Butler, C., Cook, A. L., and Harper, D.
767   B.: Comparison of mixed layer heights from airborne high spectral resolution lidar, ground-
768   based measurements, and the WRF-Chem model during CalNex and CARES, Atmos. Chem.
769   Phys., 14, 5547-5560, doi:10.5194/acp-14-5547-2014, 2014.

770 Shaw, W., Allwine, K. J., Fritz, B. G., Rutz, F. C., Rishel, J. P., and Chapman, E. G.: An evaluation
771   of the wind erosion module in DUSTRAN, Atmos. Environ., 42, 1907–1921, 2008.

772 Solomon, P. A., Crumpler, D., Flanagan, J. B., Jayanty, R. K. M., Rickman, E. E., and McDade C.
773   E.: U.S. National PM 2.5 Chemical Speciation Monitoring Networks – CSN and IMPROVE:
774   Description of Networks, J. Air Waste Manage., 64, 1410–1438,
775   doi:10.1080/10962247.2014.956904, 2014.

776 Susskind, J., Barnet, C. D., and Blaisdell, J.: Retrieval of atmospheric and surface parameters from
777   AIRS/AMSU/HSB data under cloudy conditions, IEEE Trans. Geosci. Remote Sens., 41(2),
778   390–409, doi:10.1109/TGRS.2002.808236, 2003.

779 Schuster, G. L., Dubovik, O., and Holben, B. N.: Angström exponent and bimodal aerosol size
780   distributions, J. Geophys. Res., 111, D07207, doi:10.1029/2005JD006328, 2006.

781 Tessum, C. W., Hill, J. D., and Marshall, J. D.: Twelve-month, 12 km resolution North American
782   WRF-Chem v3.4 air quality simulation: performance evaluation, Geosci. Model Dev., 8, 957-
783   973, doi:10.5194/gmd-8-957-2015, 2015.

784 Toth, T. D., Campbell, J. R., Reid, J. S., Tackett, J. L., Vaughan, M. A. and Zhang, J.: Lower
785   daytime threshold sensitivities to aerosol optical thickness in CALIPSO Level 2 products, J.
786   Geophys. Res., in review, 2017.

787 US Environmental Protection Agency, 2010: Technical Support Document: Preparation of
788   Emissions Inventories for the Version 4, 2005-based Platform, 73 pp., Office of Air Quality
789   Planning and Standards, Air Quality Assessment Division, available at:
790   https://www3.epa.gov/crossstaterule/pdfs/2005_emissions_tsd_07jul2010.pdf, 2010.

791 Wu, L., and Petty, G. W.: Intercomparison of Bulk Microphysics Schemes in Simulations of Polar
792   lows. Mon. Wea. Rev., 138, 2211-2228. doi: 10.1175/2010MWR3122.1, 2010.

793   Wu, L., Su, H. and Jiang, J. H.: Regional simulations of deep convection and biomass burning
794   over South America: 1. Model evaluations using multiple satellite data sets, J. Geophys. Res.,
795   116, D17208, doi:10.1029/2011JD016105, 2011a.

796   Wu, L., Su, H. and Jiang, J. H.: Regional simulations of deep convection and biomass burning
797   over South America: 2. Biomass burning aerosol effects on clouds and precipitation, J.
798   Geophys. Res., 116, D17209, doi:10.1029/2011JD016106, 2011b.

799   Wu, L., Su, H. and Jiang, J. H.: Regional simulations of aerosol impacts on precipitation during
800   the East Asian summer monsoon. J. Geophys. Res. Atmos., 118, doi: 10.1002/jgrd.50527,
801   2013.

802   Wu, L., Li, J.-L. F., Pi, C.-J., Yu, J.-Y., and Chen, J.-P.: An observationally based evaluation of
803   WRF seasonal simulations over the Central and Eastern Pacific, J. Geophys. Res. Atmos., 120,
804   doi:10.1002/2015JD023561, 2015.

805   Ying, Q. and Kleeman, M. J.: Regional contributions to airborne particulate matter in central
806   California during a severe pollution episode, Atmos. Environ., 43, 1218–1228, 2009.

807   Young, S.A. and Vaughan, M.A.: The retrieval of profiles of particulate extinction from Cloud–
808   Aerosol Lidar Infrared Pathfinder Satellite Observations (CALIPSO) data: algorithm
809   description. J. Atmos. Ocean. Technol. 26, 1105–1119, 2009.

810   Zaveri, R. A. and Peters, L. K.: A new lumped structure photochemical mechanism for large-scale
811   applications, J. Geophys. Res., 104, 30387–30415, 1999.

812   Zaveri, R. A., Easter, R. C., Fast, J. D., and Peters, L. K.: Model for Simulating Aerosol
813   Interactions and Chemistry (MOSAIC), J. Geophys. Res., 113, D13204,
814   doi:10.1029/2007JD008782, 2008.

815   Zhang, Y., Liu, P., Liu, X.-H., Pun, B., Seigneur, C., Jacobson, M. Z., and Wang, W.-X.: Fine
816   scale modeling of wintertime aerosol mass, number, and size distributions in central California,
817   J. Geophys. Res.-Atmos., 115, D15207, doi:10.1029/2009jd012950, 2010.

818   Zhao, C., Liu, X., Leung, L. R., Johnson, B., McFarlane, S. A., Gustafson Jr., W. I., Fast, J. D.,
819   and Easter, R.: The spatial distribution of mineral dust and its shortwave radiative forcing over
820   North Africa: modeling sensitivities to dust emissions and aerosol size treatments, Atmos.
821   Chem. Phys., 10, 8821–8838, doi: 10.5194/acp-10-8821-2010, 2010.

822 Zhao, C., Liu, X., Ruby Leung, L., and Hagos, S.: Radiative impact of mineral dust on monsoon
823   precipitation variability over West Africa, Atmos. Chem. Phys., 11, 1879–1893,
824   doi:10.5194/acp-11-1879-2011, 2011.

825 Zhao, C., Chen, S., Leung, L. R., Qian, Y., Kok, J. F., Zaveri, R. A., and Huang, J.: Uncertainty in
826   modeling dust mass balance and radiative forcing from size parameterization, Atmos. Chem.
827   Phys., 13, 10733-10753, doi:10.5194/acp-13-10733-2013, 2013a.

828 Zhao, C., Leung, L. R., Easter, R., Hand, J., and Avise, J.: Characterization of speciated aerosol
829   direct radiative forcing over California, J. Geophys. Res., 118, 2372–2388, doi:
830   10.1029/2012JD018364, 2013b.

831 Zhao, C., Hu, Z., Qian, Y., Ruby Leung, L., Huang, J., Huang, M., Jin, J., Flanner, M. G., Zhang,
832   R., Wang, H., Yan, H., Lu, Z., and Streets, D. G.: Simulating black carbon and dust and their
833   radiative forcing in seasonal snow: a case study over North China with field campaign
834   measurements, Atmos. Chem. Phys., 14, 11475-11491, doi:10.5194/acp-14-11475-2014,
835   2014.

836 **List of Table**

837 Table 1. Experiment description

Experiment ID	Experiment description
20km	Simulation with the GOCART dust scheme at 20 km horizontal resolution.
20km_D2	Same as 20km, but with the DUSTRAN dust scheme.
20km_P7	Same as 20km_D2, but with the ACM2 PBL scheme.
4km	Same as 20km, but at 4 km horizontal resolution.
4km_D2	Same as 4km, but with the DUSTRAN dust scheme.

838

839   Table 2. Correlation with observations for different species at Fresno, CA

Species	20km	4km	4km_D2	20km_D2	20km_P7
$PM_{2.5}$	0.89	0.90	0.86	0.78	0.03
$PM_{2.5}\_NO_3$	0.94	0.95	0.94	0.94	0.91
$PM_{2.5}\_NH_4$	0.97	0.96	0.96	0.98	0.96
$PM_{2.5}\_OM$	0.93	0.93	0.94	0.93	0.91
$PM_{2.5}\_EC$	0.98	0.98	0.98	0.98	0.96
$PM_{2.5}\_SO_4$	0.63	-0.16	-0.14	0.61	0.63
$PM_{2.5}\_dust$	-0.55	-0.50	0.48	0.55	0.36
PM_{10}	-0.25	-0.23	-0.08	0.01	-0.03

840

841   Table 3. Surface aerosol mass (μg m^{-3}) for different species at Fresno, CA

Species	Cold season						Warm season					
	OBS	20km	4km	4km_D2	20km_D2	20km_P7	OBS	20km	4km	4km_D2	20km_D2	20km_P7
PM$_{2.5}$	16.84	13.71	21.38	22.48	14.90	13.77	8.44	4.91	6.29	12.85	10.12	14.85
PM$_{2.5\_}$NO$_3$	5.43	6.36	9.54	9.22	6.22	3.16	0.84	0.55	0.69	0.79	0.66	0.57
PM$_{2.5\_}$NH$_4$	1.42	1.97	2.99	2.88	1.91	0.98	0.40	0.19	0.24	0.20	0.16	0.13
PM$_{2.5\_}$OM	5.39	0.92	2.07	2.07	0.93	1.04	2.47	0.49	0.87	0.87	0.50	0.55
PM$_{2.5\_}$EC	1.08	0.52	1.12	1.13	0.52	0.58	0.32	0.27	0.49	0.49	0.27	0.30
PM$_{2.5\_}$SO$_4$	0.87	0.53	0.82	0.81	0.53	0.46	1.04	0.54	0.61	0.60	0.53	0.49
PM$_{2.5\_}$dust	0.90	0.11	0.11	1.65	1.50	4.18	2.08	0.04	0.03	6.49	5.16	10.05
PM$_{10}$	31.55	14.93	22.81	28.32	20.10	24.52	34.82	7.08	8.69	38.12	30.19	48.02

842

843 Supplementary Table 1. Correlation with surface observations for meteorological variables at
844 Fresno, CA

	4km_D2	20km_D2	20km_P7
T	0.94	0.94	0.94
RH	0.98	0.98	0.96
Wind	0.83	0.84	0.85
Rain	0.97	0.97	0.97

845

846   Supplementary Table 2. Bias for surface meteorological variables at Fresno, CA

	Cold season			Warm season		
	4km_D2	20km_D2	20km_P7	4km_D2	20km_D2	20km_P7
T (K)	3.89	3.56	3.69	2.44	1.50	1.35
RH (%)	-9.78	-14.55	-19.35	-9.48	-9.32	-11.16
Wind (m/s)	-0.67	-1.00	-1.05	0.78	-0.16	-0.49
Rain (mm/day)	-0.15	0.14	-0.03	-0.06	-0.03	-0.04

847

848 **List of Figures**
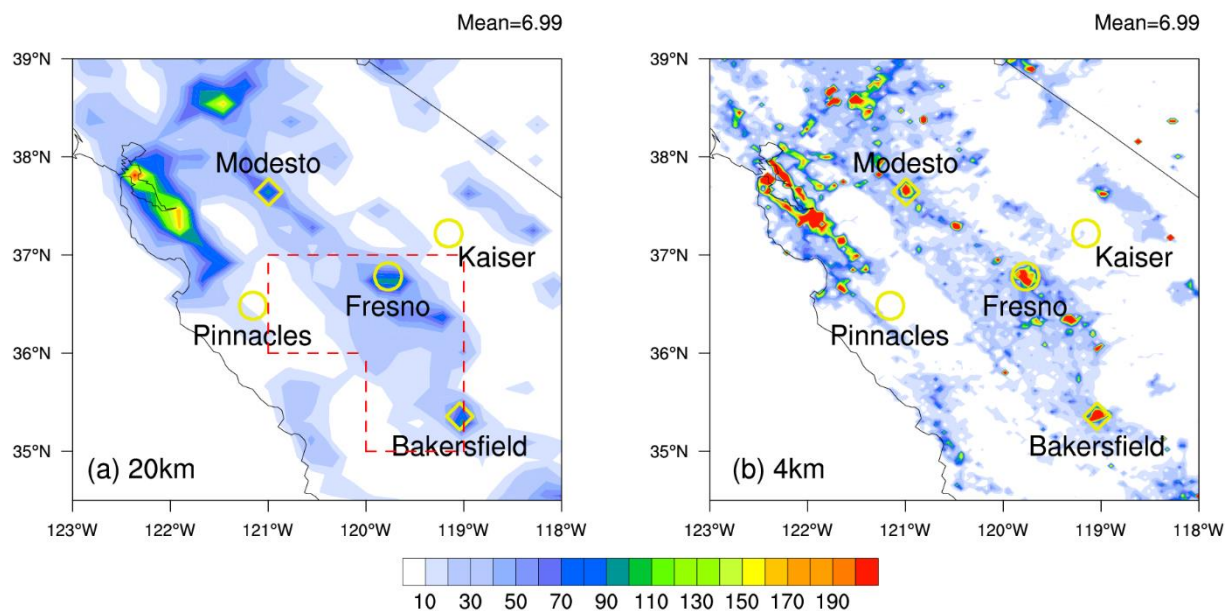
849

850 Figure 1. Daily mean anthropogenic $PM_{2.5}$ emission rate ($\mu g\ m^{-2}\ hr^{-1}$) at (a) 20km and (b) 4km

851 simulation. Domain-averaged emission rate is shown at right corner of each figure. Red dashed

852 lines in Figure 1a represent the region used for the domain averages in the discussions. Yellow

853 circle: IMPROVE site; yellow diamond: EPA CSN site. Three urban sites: Fresno, Bakersfield and

854 Modesto; two rural sites: Pinnacles and Kaiser.
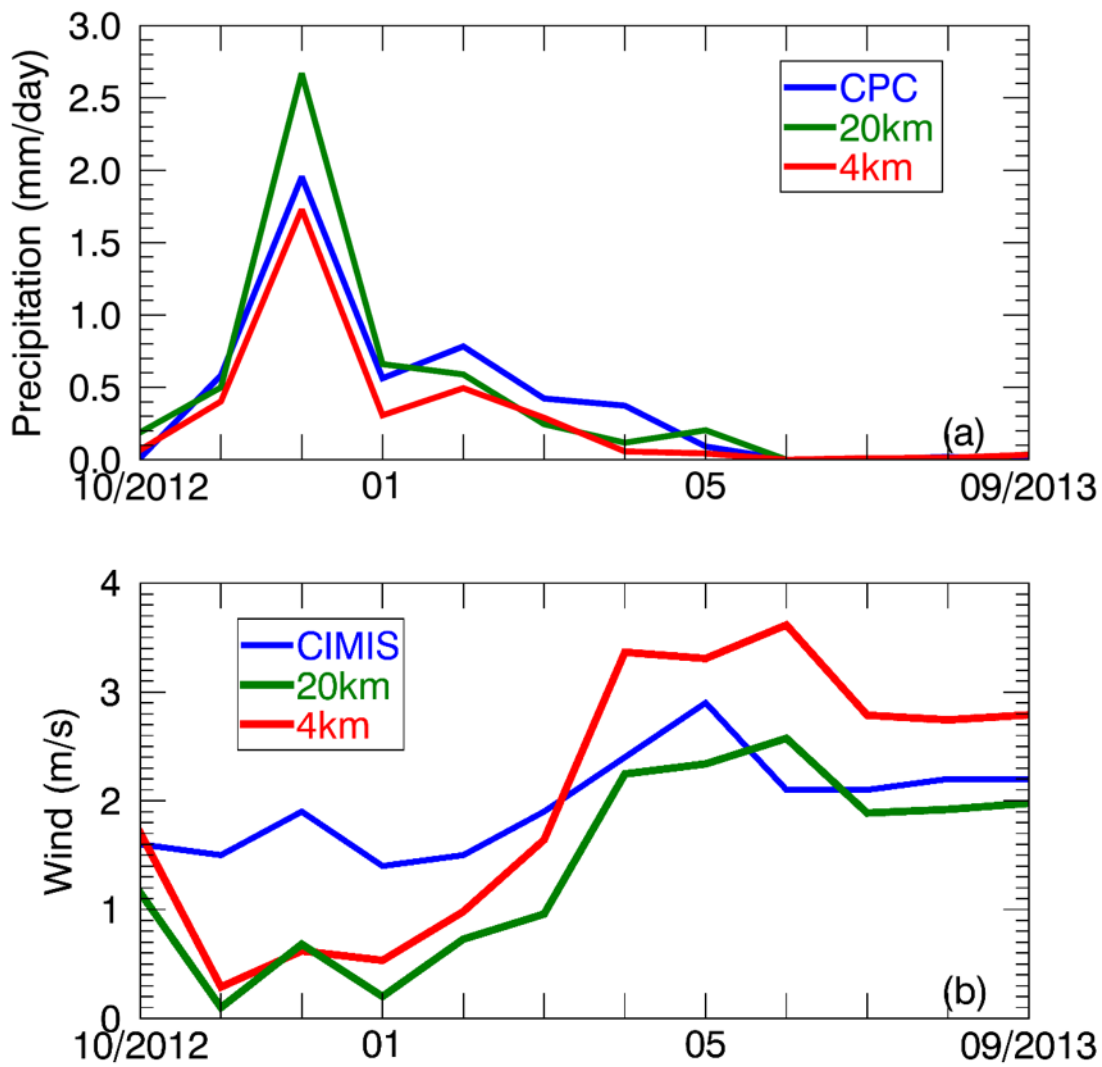
855

856 Figure 2. (a) Monthly precipitation (mm/day) from CPC, 20km and 4km; (b) monthly wind speed
857 (m/s) from CIMIS, 20km and 4km. 4km_D2 (not shown) is similar to 4km.
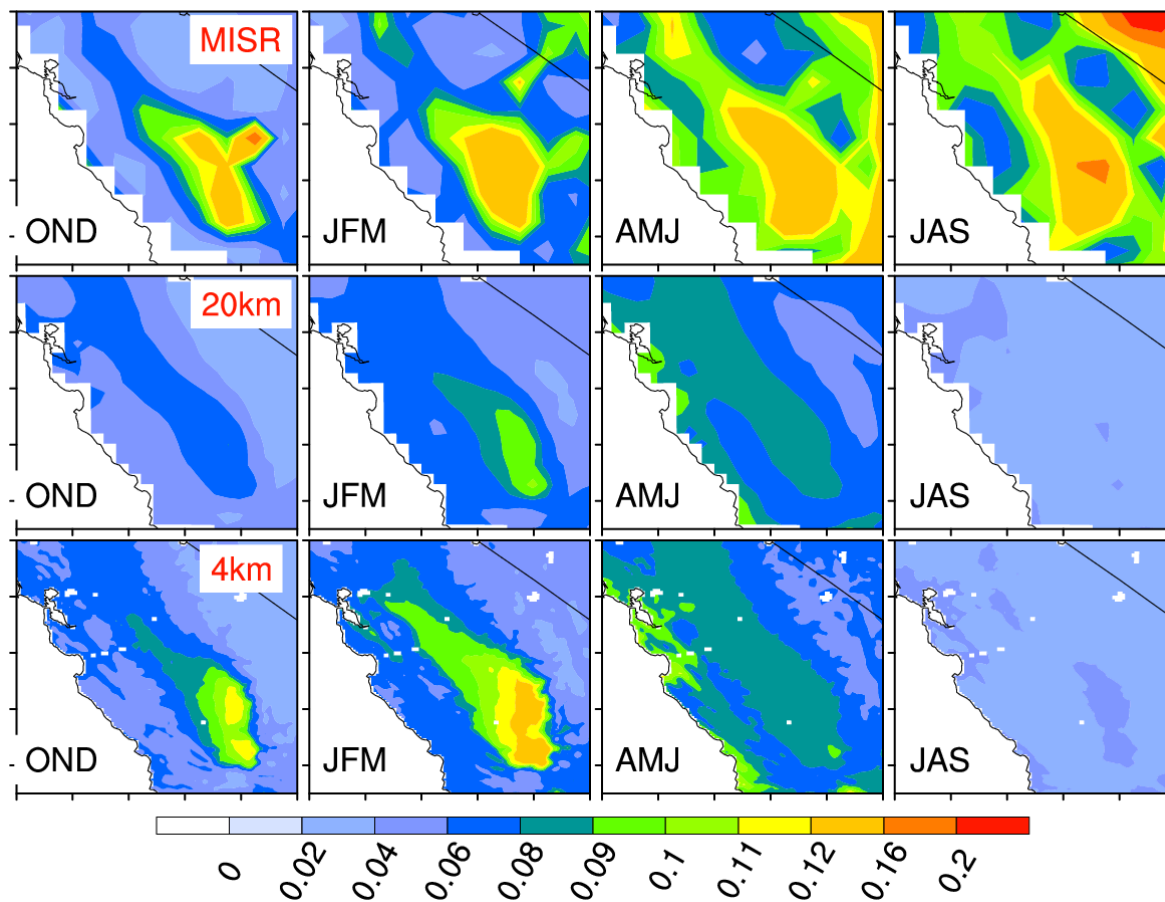
858

859 Figure 3. Spatial distribution of seasonal mean 550 nm AOD from MISR and the WRF-Chem

860 (20km and 4km) simulations in WY2013. OND: October-November-December; JFM: January-

861 February-March; AMJ: April-May-June; JAS: July-August-September.

862
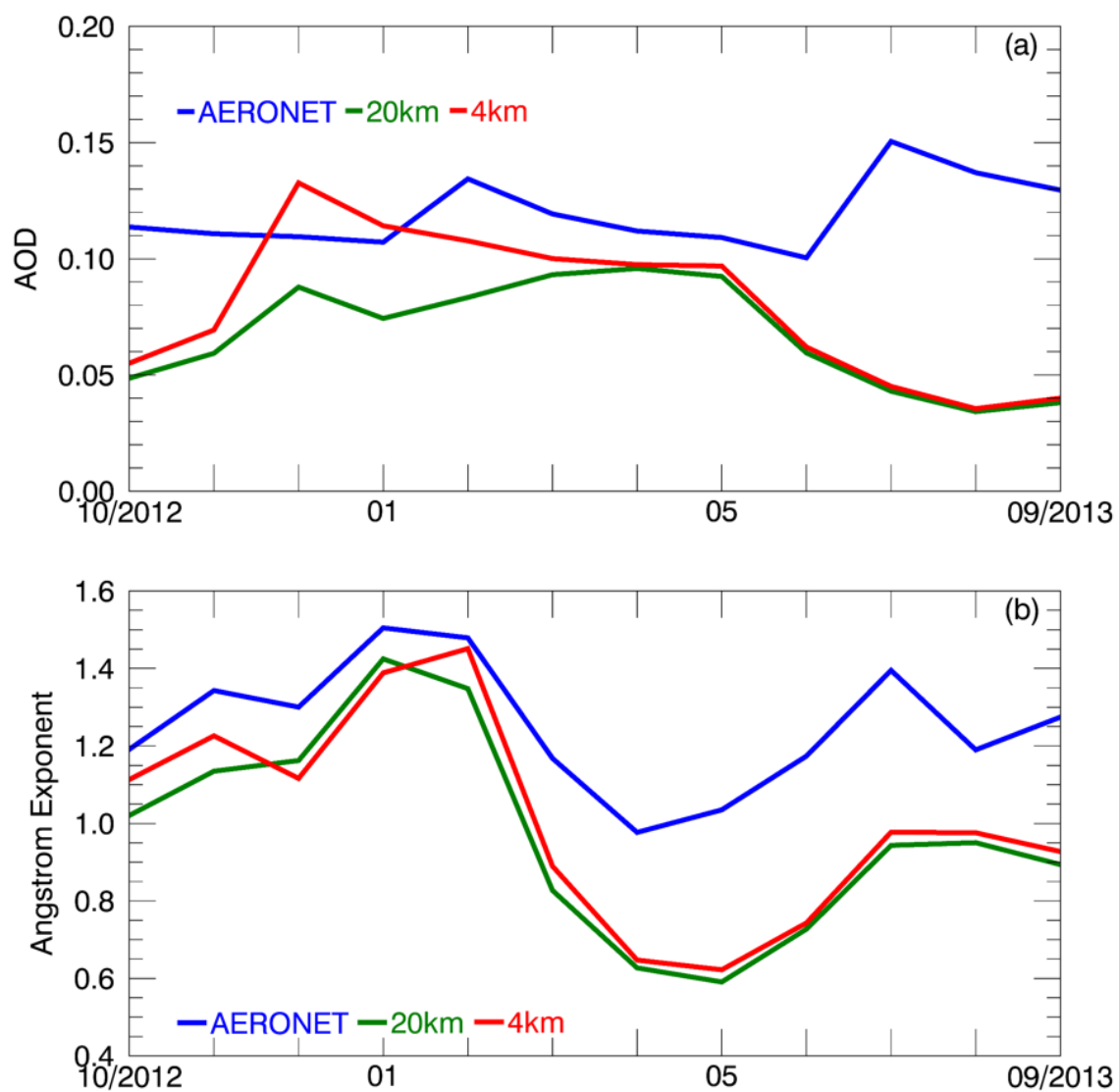
863

864   Figure 4. (a) Monthly mean 550 nm AOD; (b) monthly mean 400-600 nm Ångström exponent at

865   Fresno, CA from October 2012 to September 2013.
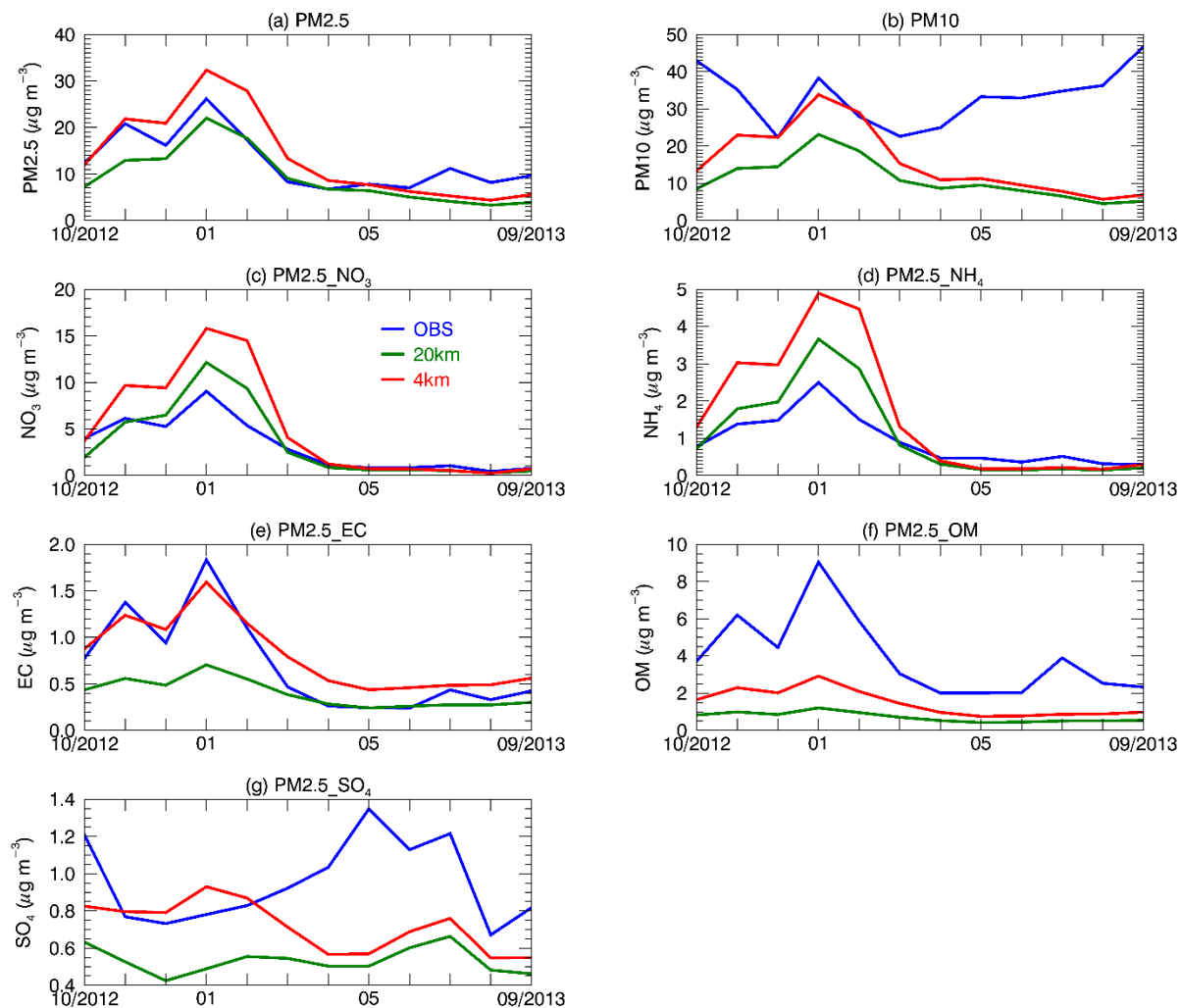
Figure 5. Aerosol mass (μg m^{-3}) for different species from OBS, the 20km and 4km simulations at Fresno, CA. NH$_4$ observations are from EPA; other observations are from IMPROVE. PM$_{2.5}$_NO$_3$ represents NO$_3$ with diameter $\leq$ 2.5 μm. Similar definition for NH$_4$, EC, OM and SO$_4$ in the figures.
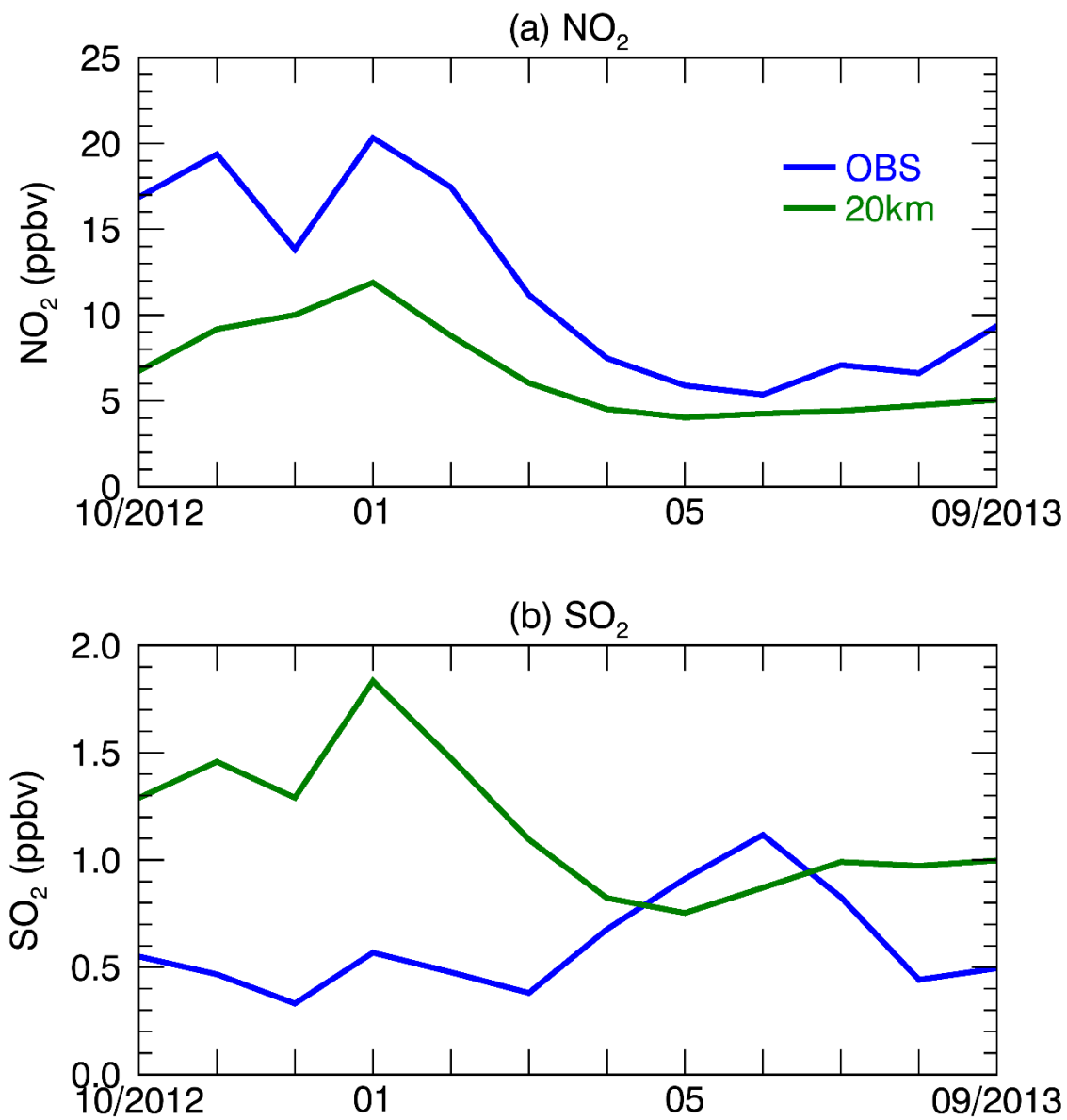
870

871 Figure 6. (a) NO$_2$ and (b) SO$_2$ from EPA (OBS) and the 20km run at Fresno, CA.
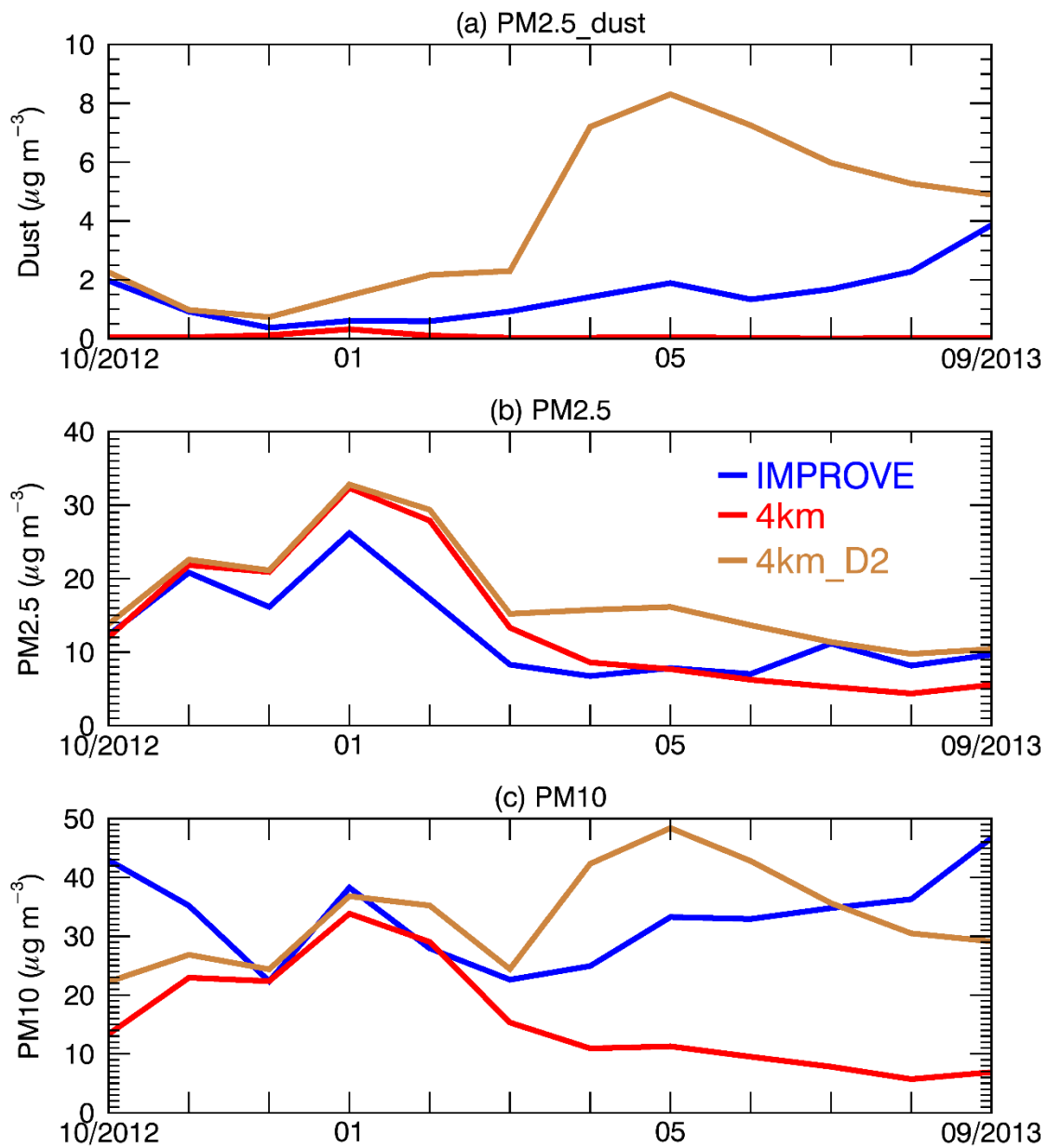
872

873   Figure 7. (a) PM$_{2.5}$_dust; (b) PM$_{2.5}$; and (c) PM$_{10}$ from IMPROVE, the 4km and 4km_D2

874   simulations at Fresno, CA.
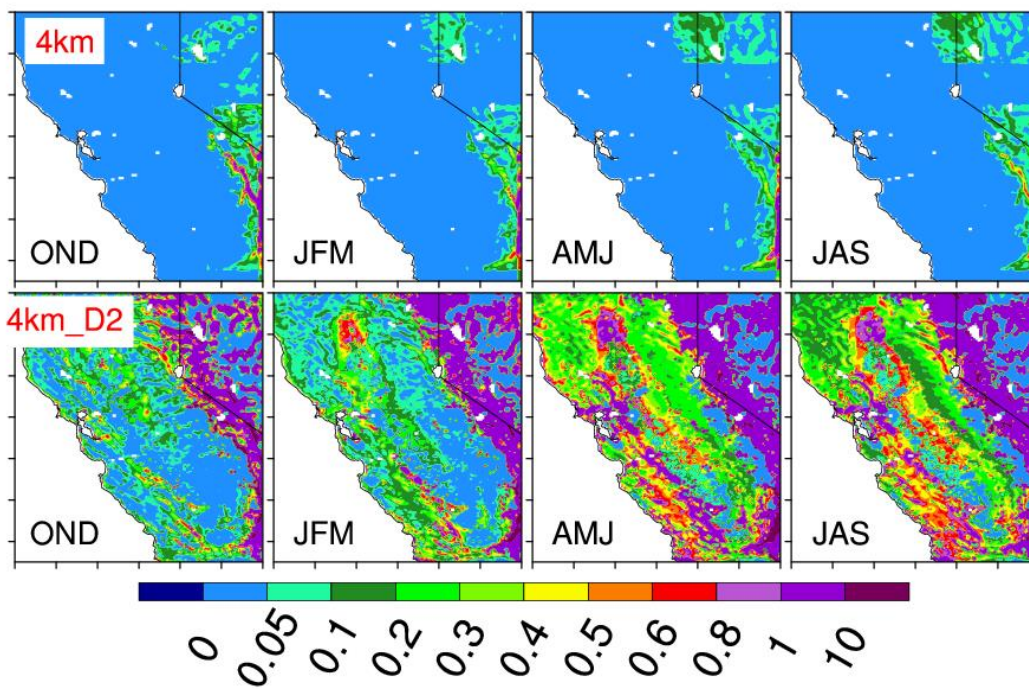
875

876   Figure 8. Mean dust emission rate (µg m^{-2} s^{-1}) from the 4km and 4km_D2 runs.
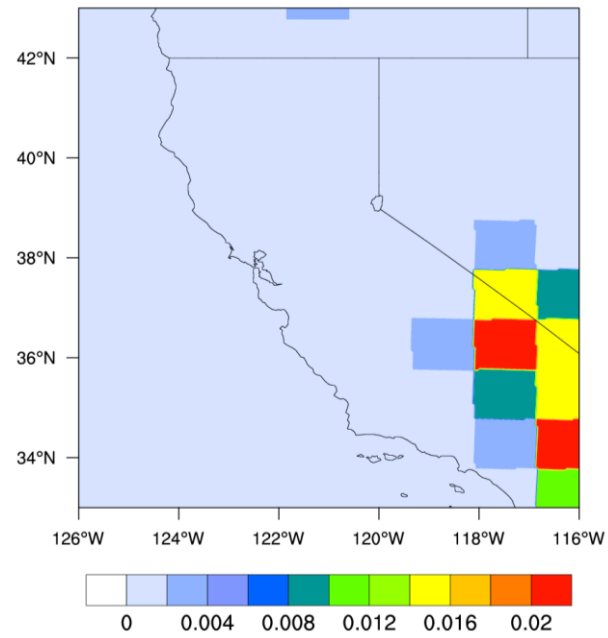
877

878   Figure 9. Fraction of erodible surface in the GOCART dataset used in this study.

879
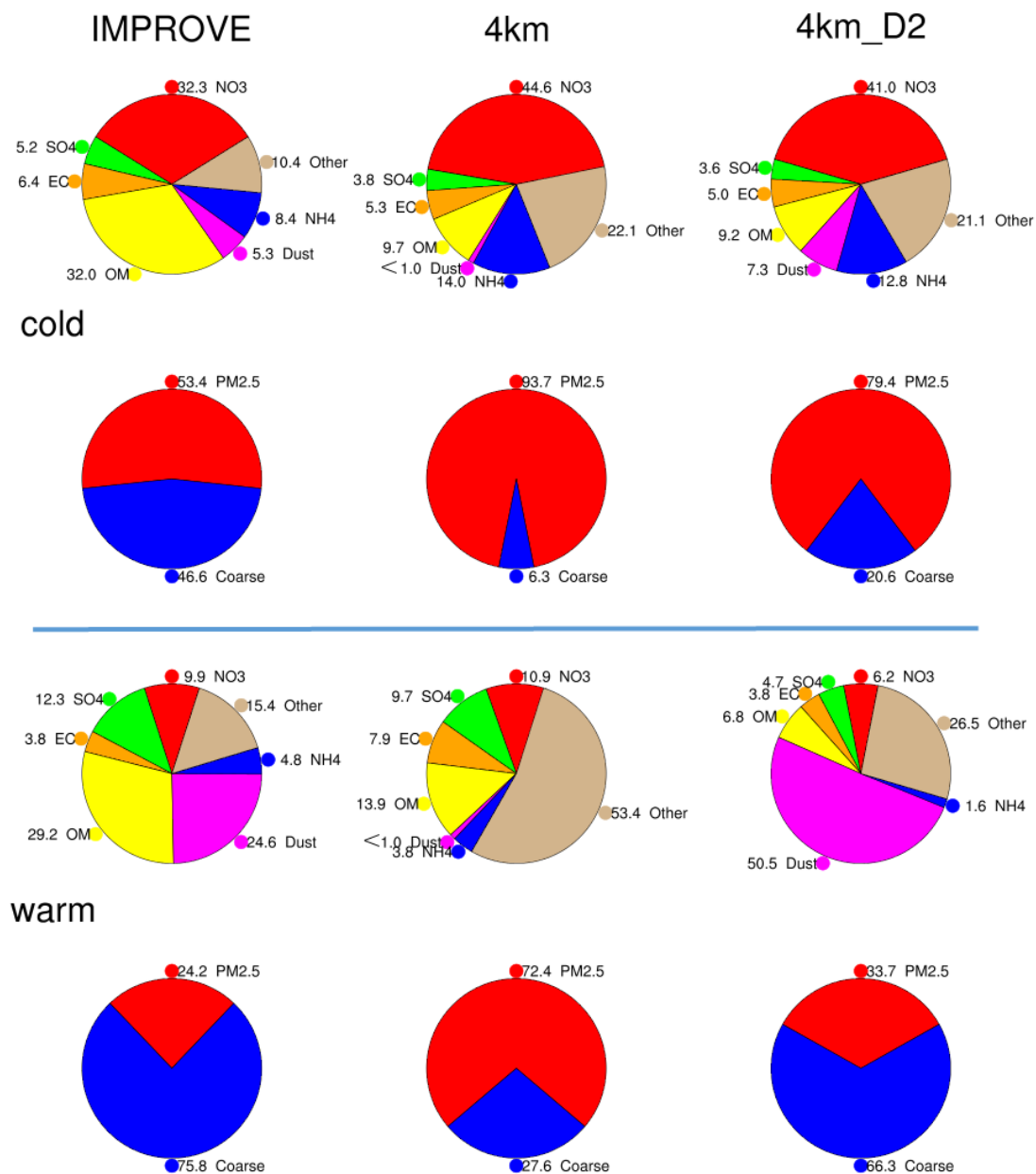
Figure 10. Relative contribution (%) of aerosol species from IMPROVE and the WRF-Chem (4km and 4km_D2) simulations at Fresno, CA in WY2013. (Panel 1) Contribution to $PM_{2.5}$ in the cold season; (Panel 2) relative contribution of $PM_{2.5}$ and coarse mass (CM) to PM_{10} in the cold season; (Panel 3) same as Panel 1 but in the warm season; (Panel 4) same as Panel 2 but in the warm season. "Other" refers to the difference of $PM_{2.5}$ total mass and specified $PM_{2.5}$ (NO_3, NH_4, OM, EC, SO_4 and dust).
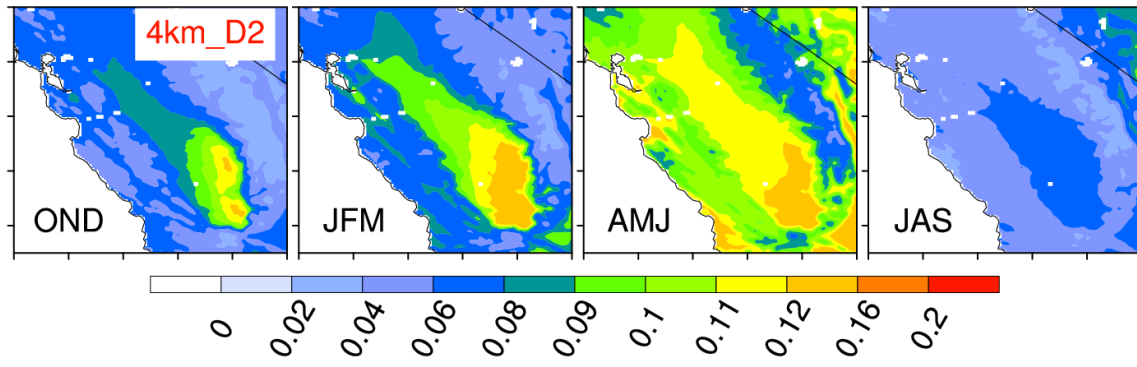
886

887   Figure 11. Spatial distribution of seasonal mean 550 nm AOD from the 4km_D2 run in WY2013.
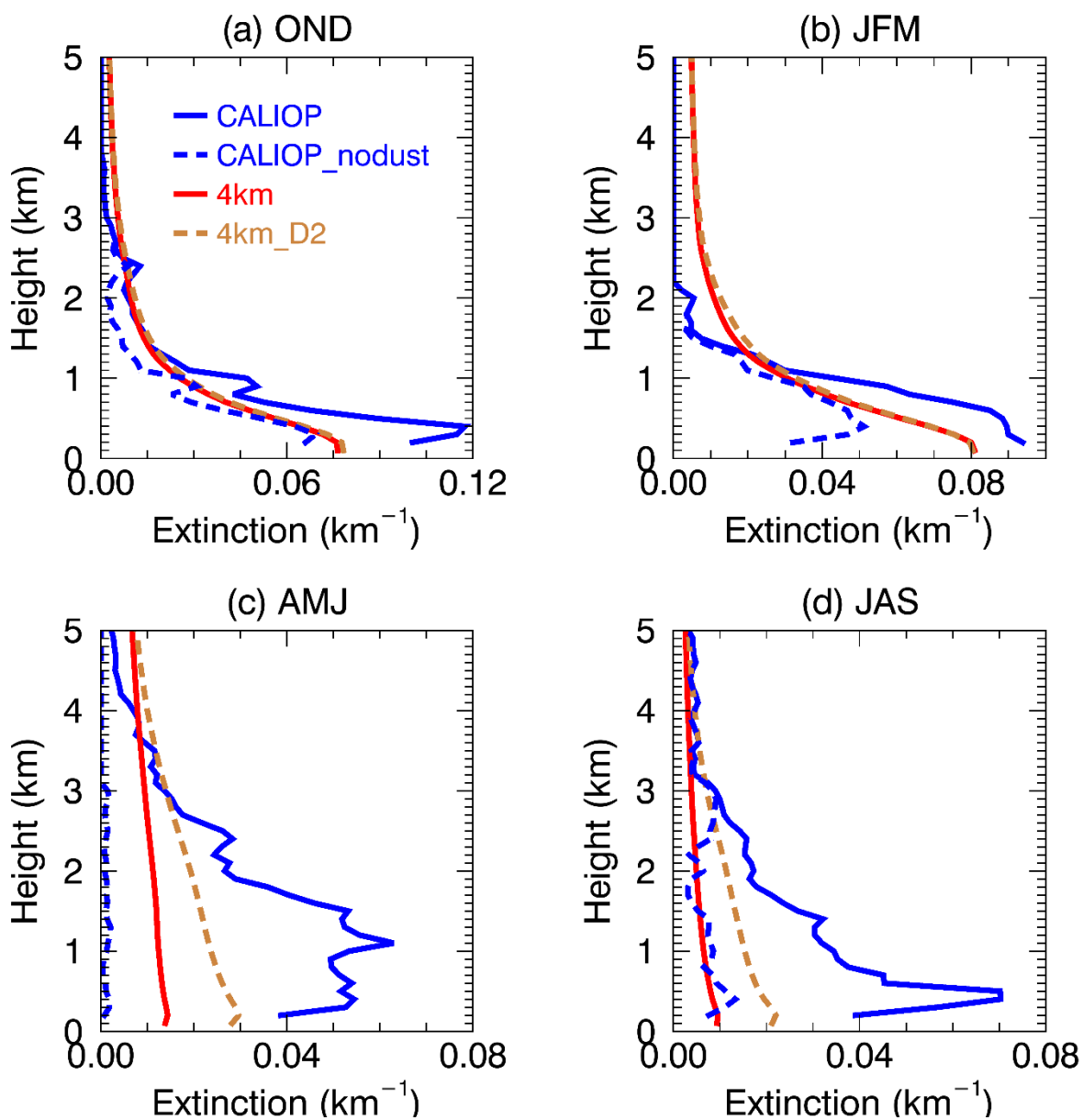
888

889 Figure 12. Vertical distribution of seasonal mean 532 nm aerosol extinction coefficient (km⁻¹)

890 from CALIOP (blue) and the WRF-Chem (4km and 4km_D2) simulations over the red box

891 region in Fig. 1a in WY2013. Blue dashed lines (CALIOP_nodust) represent the CALIOP

892 profiles without dust (dust and polluted dust).

893
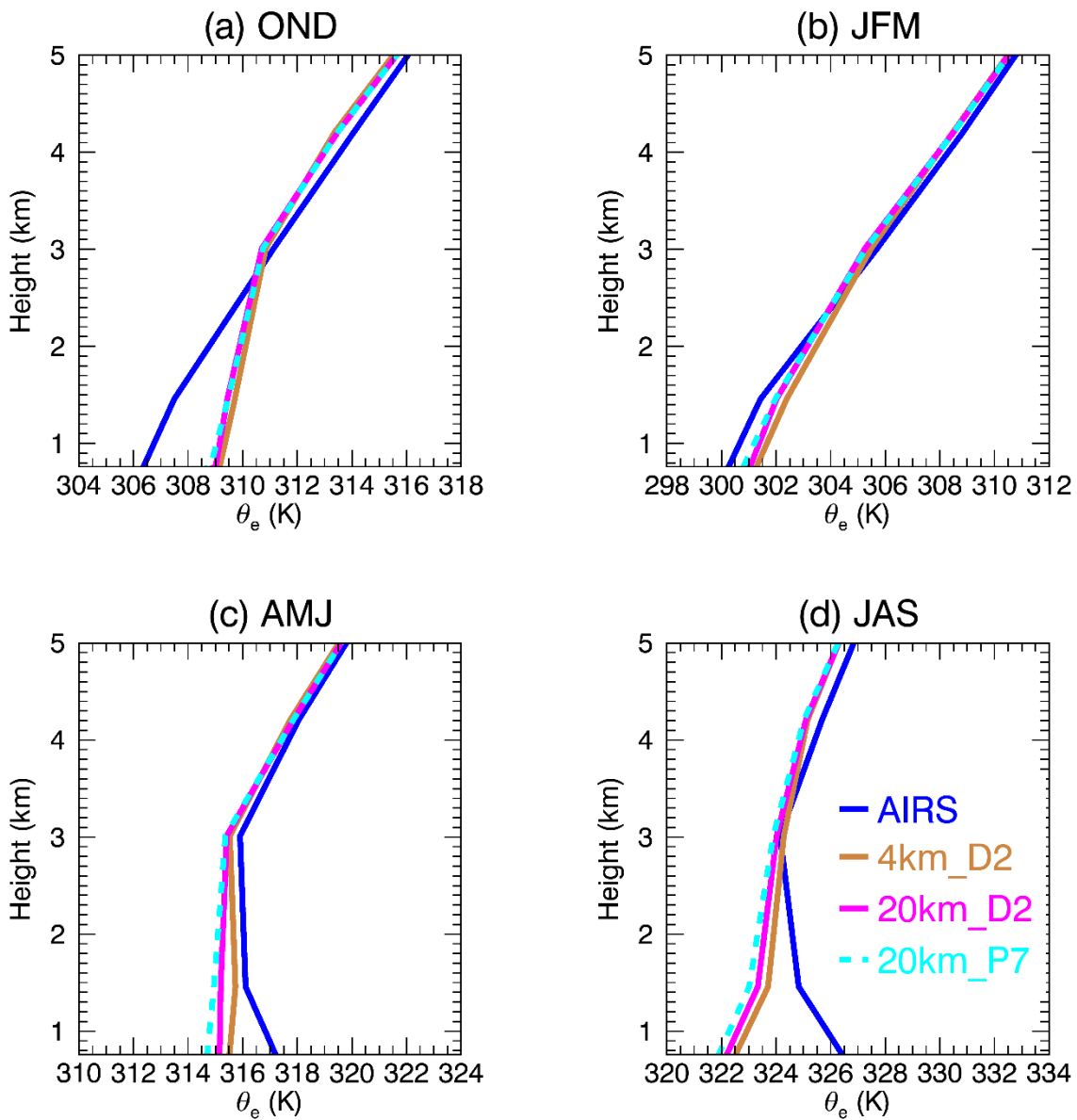
Figure 13. Vertical distribution of season mean equivalent potential temperature (θ_e; K) from AIRS

and the WRF-Chem (4km_D2, 20km_D2 and 20km_P7) simulations over the red box region in

Fig. 1a in WY2013. The 4km run (not shown) is similar to the 4km_D2 run.
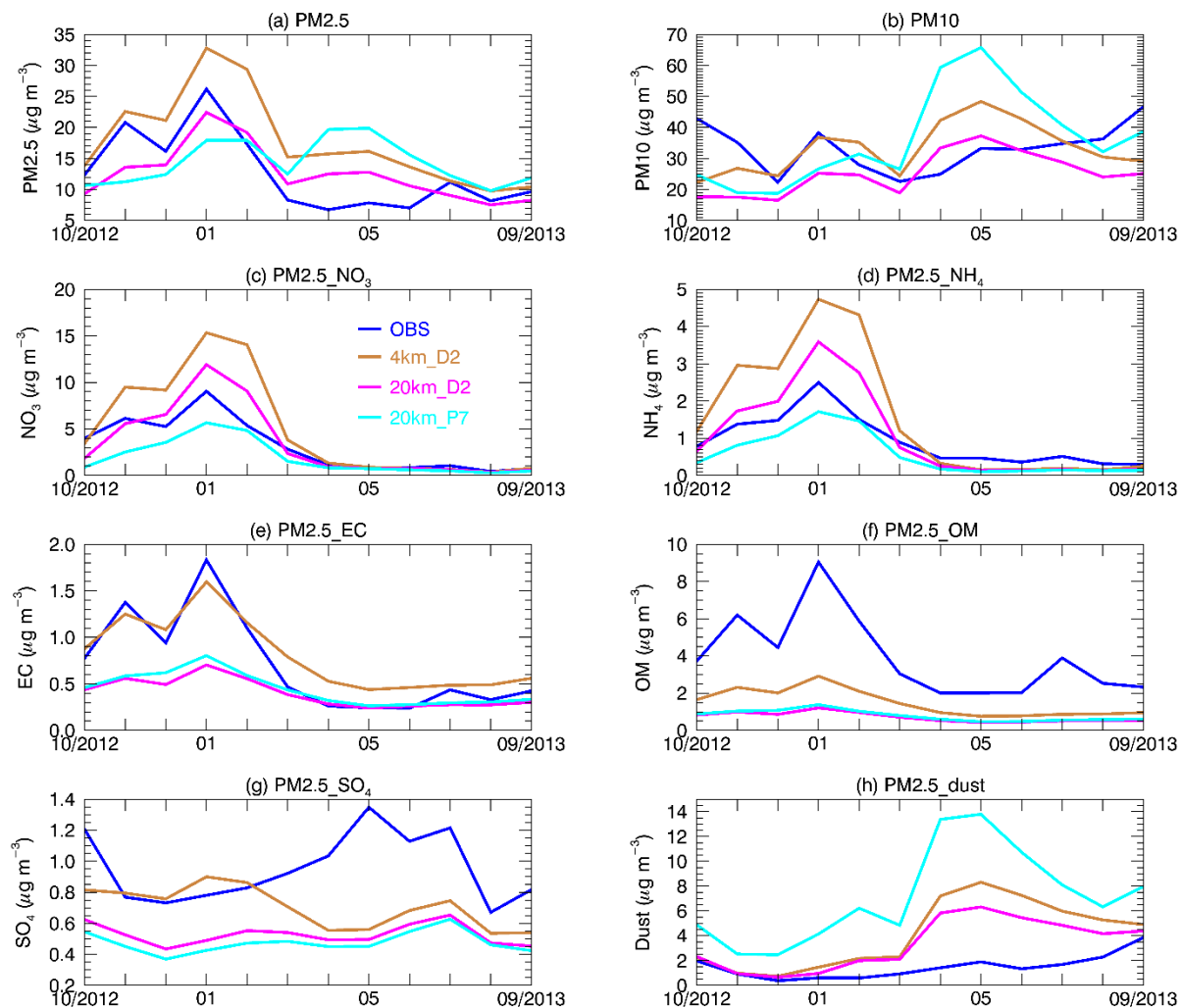
Figure 14. Aerosol mass (μg m^{-3}) for different species from OBS, the 4km_D2, 20km_D2 and 20km_P7 simulations at Fresno, CA. NH$_4$ observations are from EPA; other observations are from IMPROVE. PM$_{2.5}$_NO$_3$ represents NO$_3$ with diameter ≤ 2.5 μm. Similar definition for NH$_4$, EC, OM, SO$_4$ and dust in the figures.
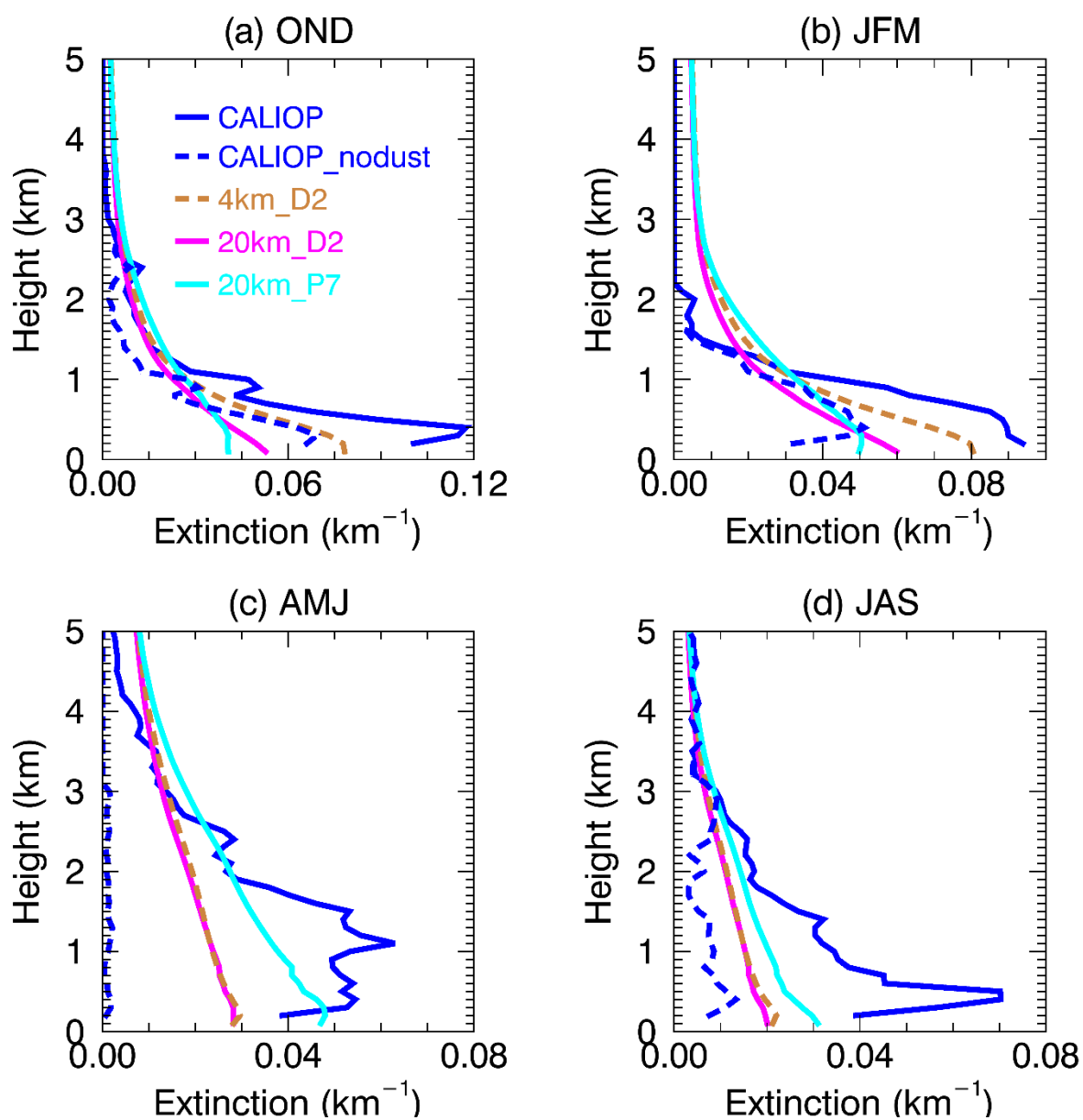
Figure 15. Vertical distribution of seasonal mean 532 nm aerosol extinction coefficient (km^{-1}) from CALIOP, CALIOP_nodust, and the WRF-Chem (4km_D2, 20km_D2 and 20km_P7) simulations over the red box region in Fig. 1a in WY2013.
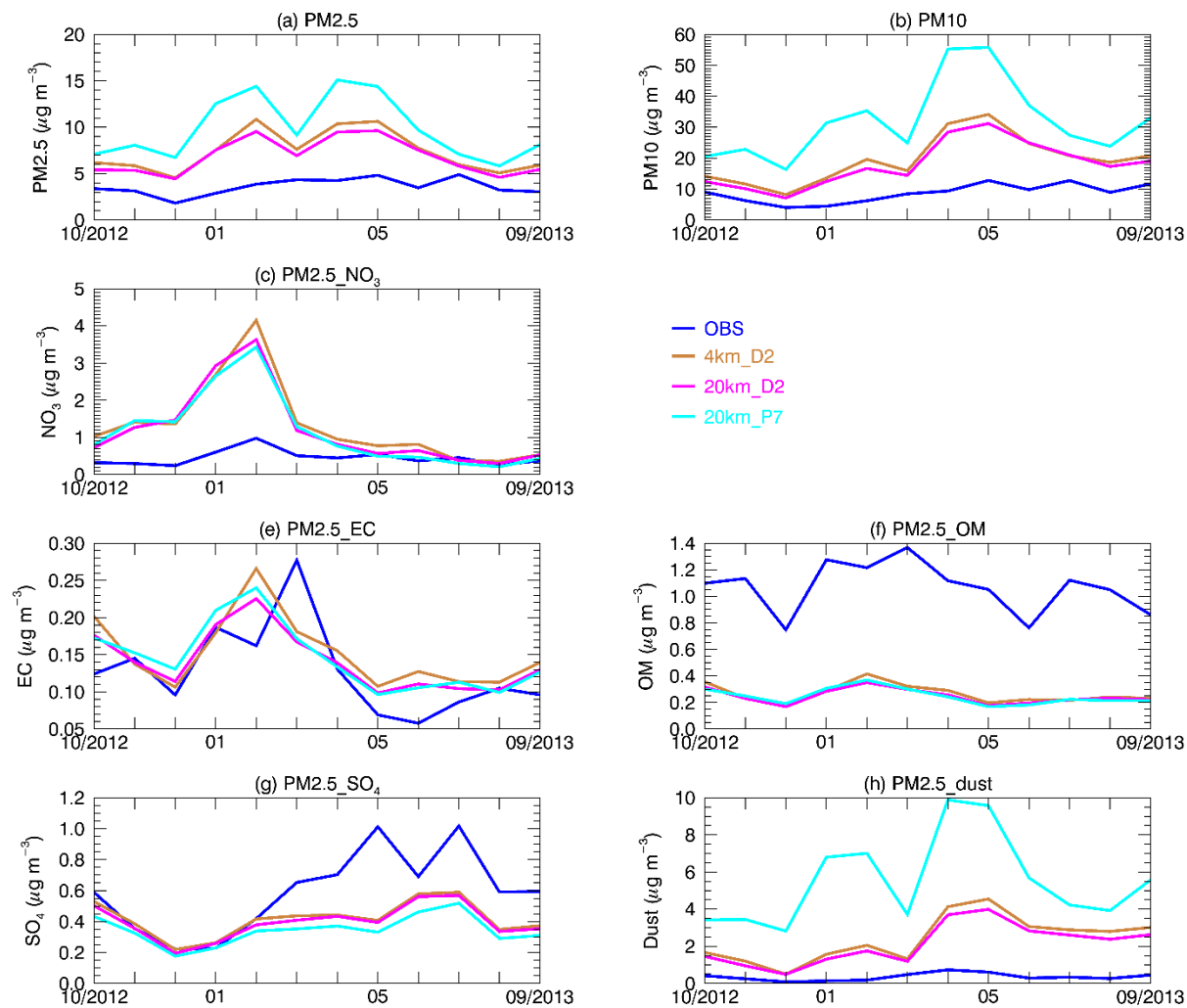
Figure 16. Aerosol mass (μg m^{-3}) for different species from IMPROVE (OBS), the 4km_D2, 20km_D2 and 20km_P7 simulations at Pinnacles, CA.
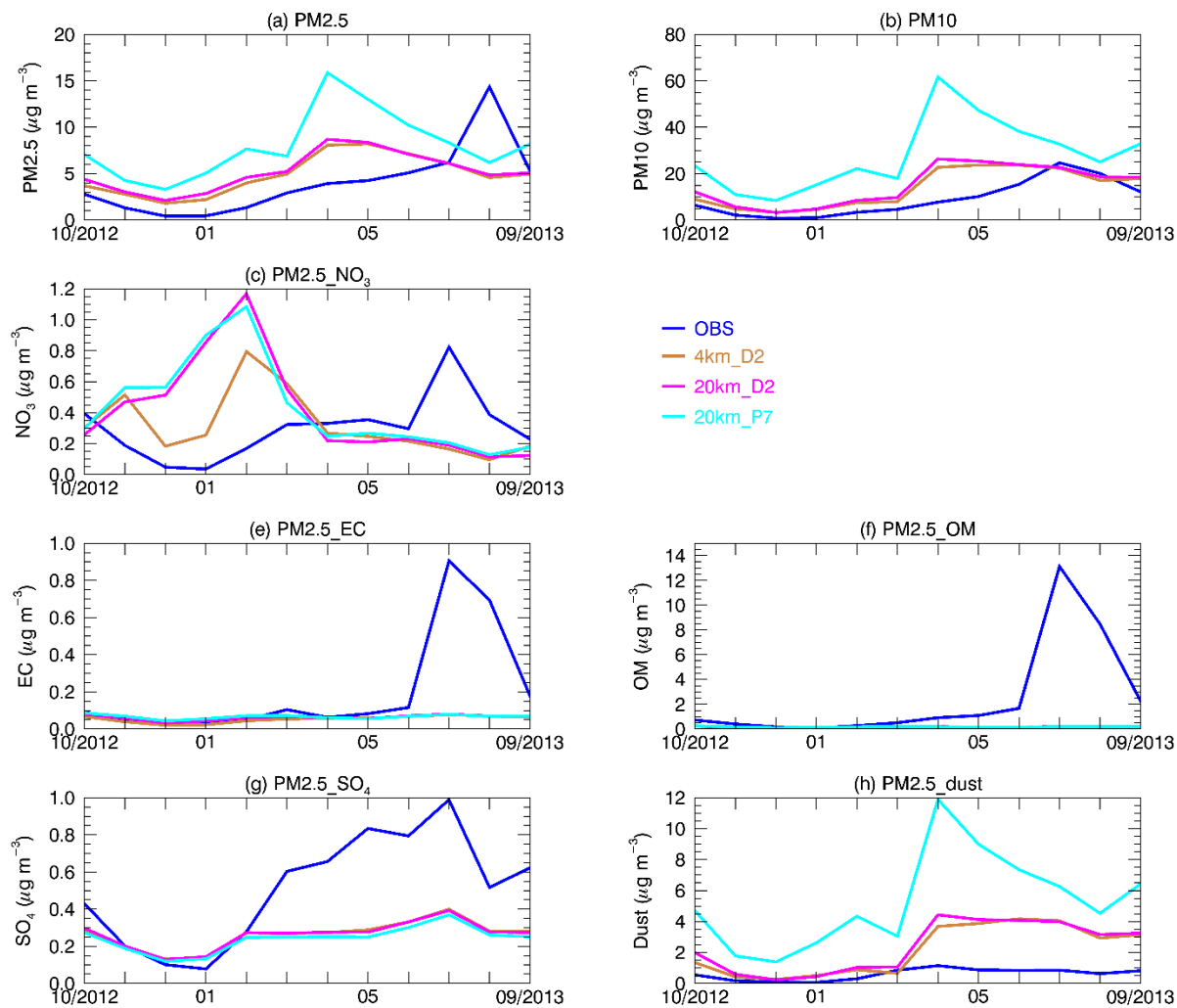
Figure 17. Aerosol mass (μg m⁻³) for different species from IMPROVE (OBS), the 4km_D2, 20km_D2 and 20km_P7 simulations at Kaiser, CA.

912
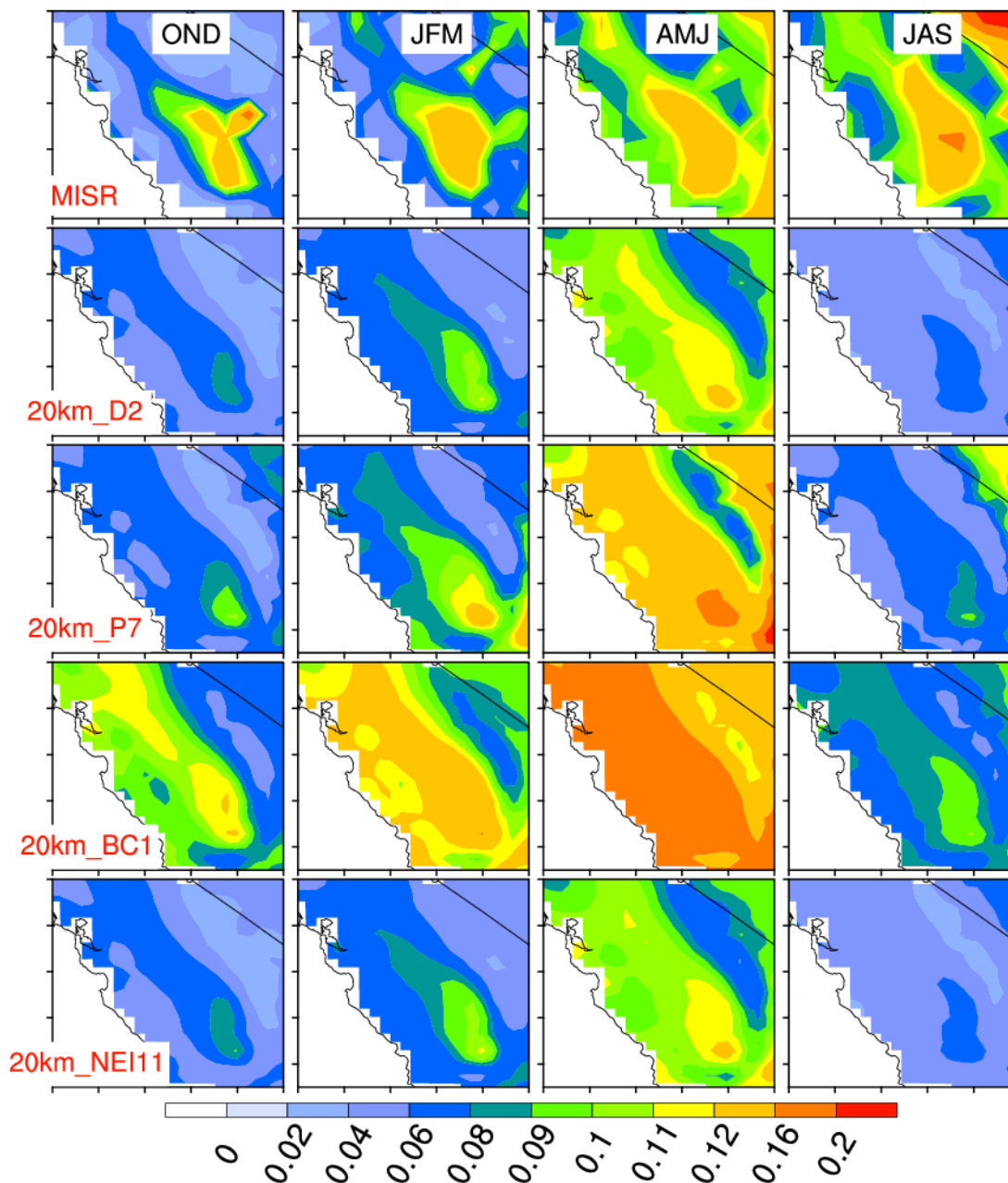
Supplementary Figure 1. Spatial distribution of seasonal mean 550 nm AOD from MISR and the WRF-Chem (20km_D2, 20km_P7, 20km_BC1 and 20km_NEI11) simulations in WY2013. OND: October-November-December; JFM: January-February-March; AMJ: April-May-June; JAS: July-August-September. The 20km_BC1 run is the same as the 20km_D2 run except that chemical boundary conditions use MOZART-4 original data. The 20km_NEI11 run is the same as the 20km_D2 run except with NEI11 anthropogenic emissions.
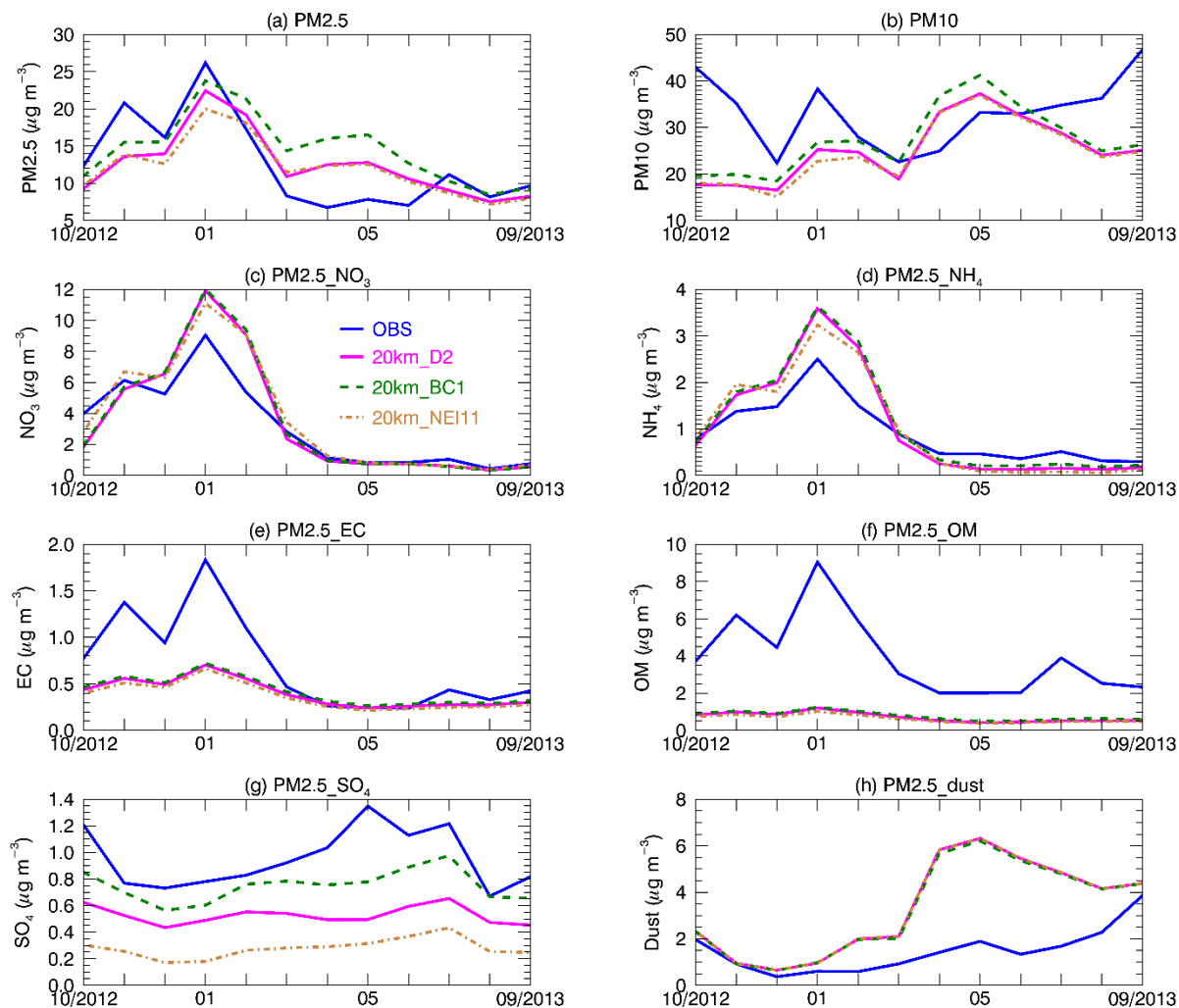
919

920   Supplementary Figure 2. Aerosol mass (μg m^{-3}) for different species from OBS, the 20km_D2,

921   20km_BC1 and 20km_NEI11 simulations at Fresno, CA. NH$_4$ observations are from EPA; other

922   observations are from IMPROVE. PM$_{2.5}$_NO$_3$ represents NO$_3$ with diameter $\leq$ 2.5 μm. Similar

923   definition for NH$_4$, EC, OM, SO$_4$ and dust in the figures.
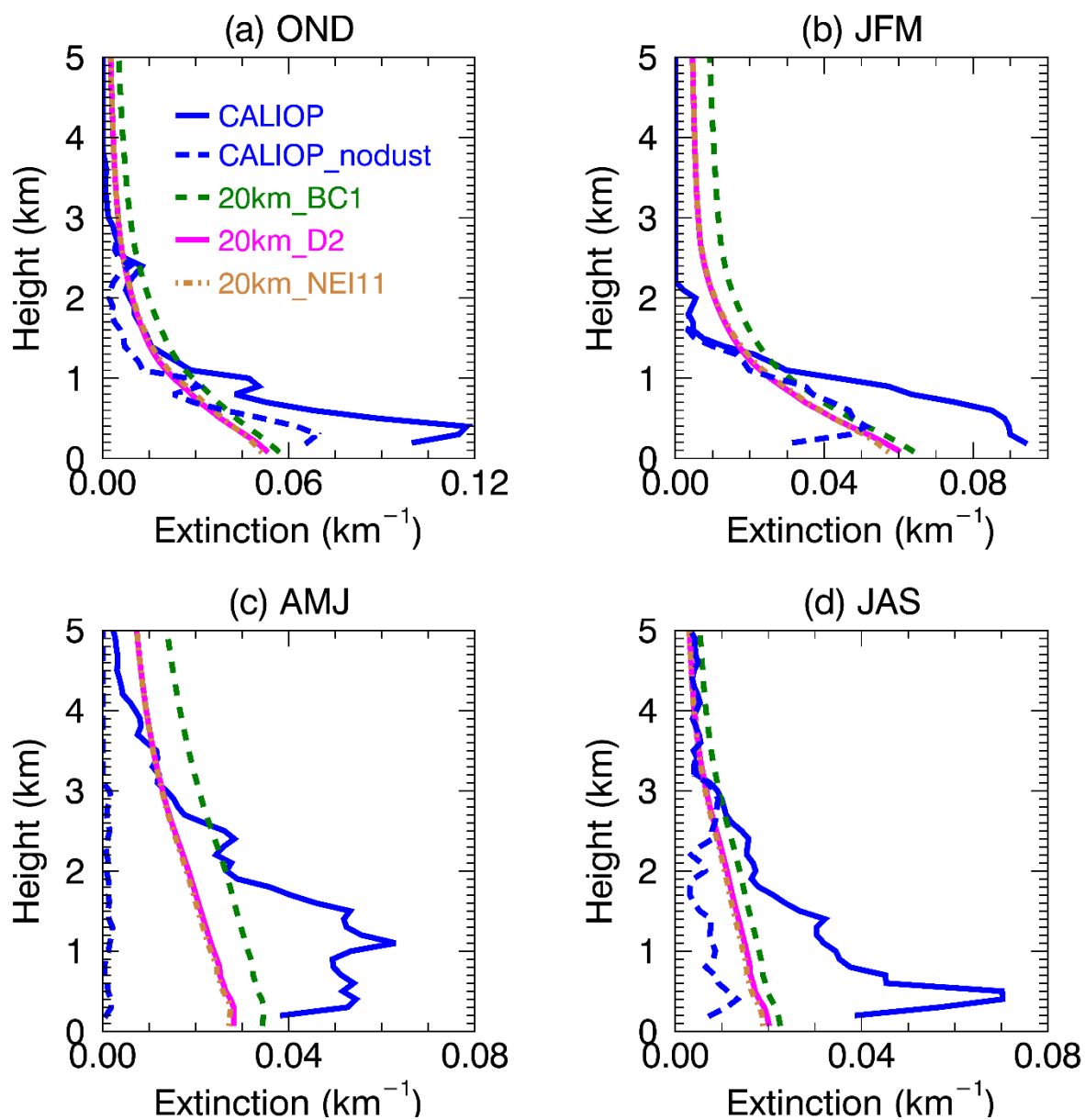
924
925 Supplementary Figure 3. Vertical distribution of seasonal mean 532 nm aerosol extinction
926 coefficient (km-1) from CALIOP, CALIOP_nodust, and the WRF-Chem (20km_D2, 20km_BC1
927 and 20km_NEI11) simulations over the red box region in Fig. 1a in WY2013.
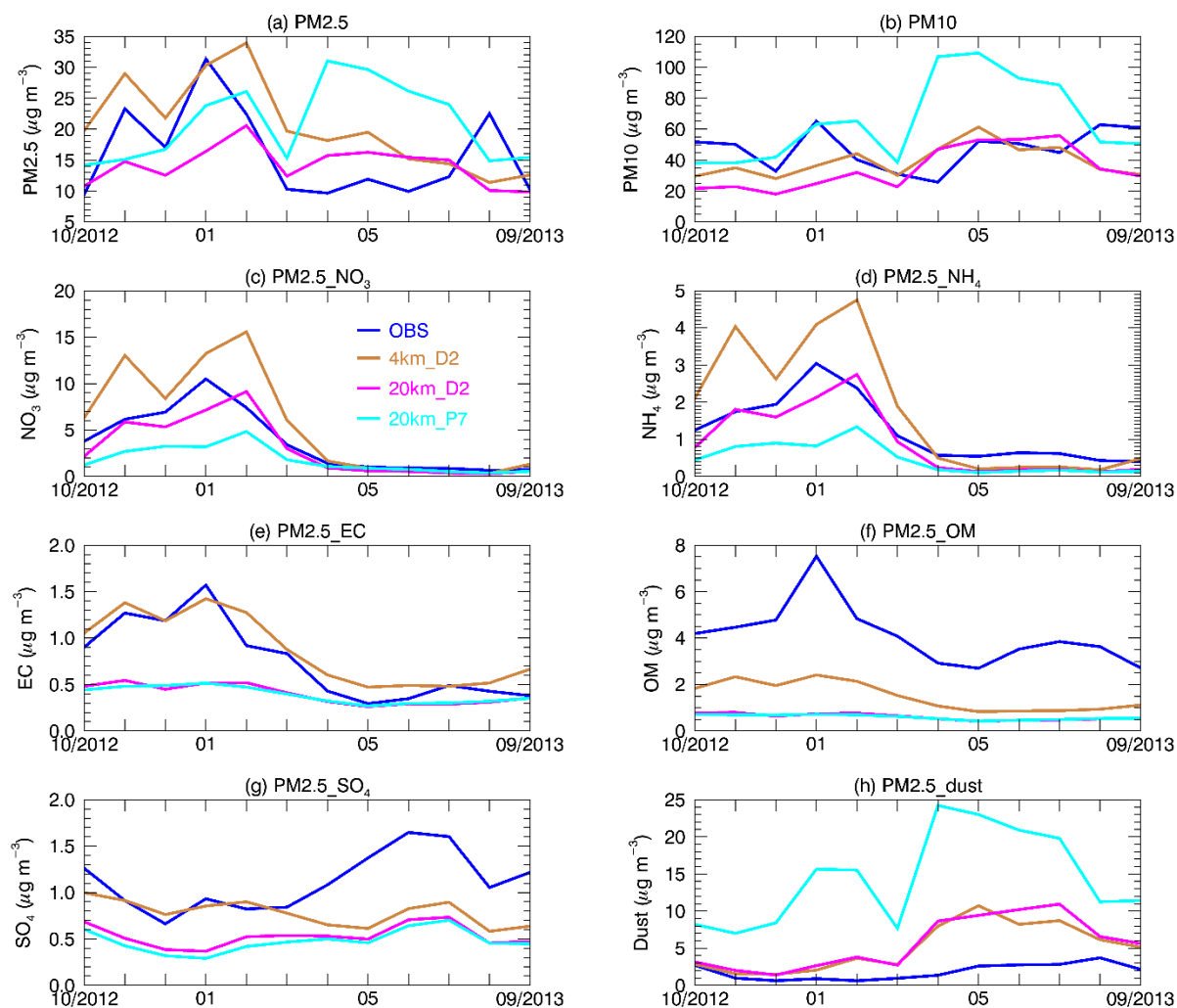
928

929 Supplementary Figure 4. Aerosol mass (μg m⁻³) for different species from EPA CSN (OBS), the

930 4km_D2, 20km_D2 and 20km_P7 simulations at Bakersfield, CA. PM$_{2.5}$_NO$_3$ represents NO$_3$

931 with diameter ≤ 2.5 μm. Similar definition for SO$_4$, EC, OM, NH$_4$ and dust in the figures.
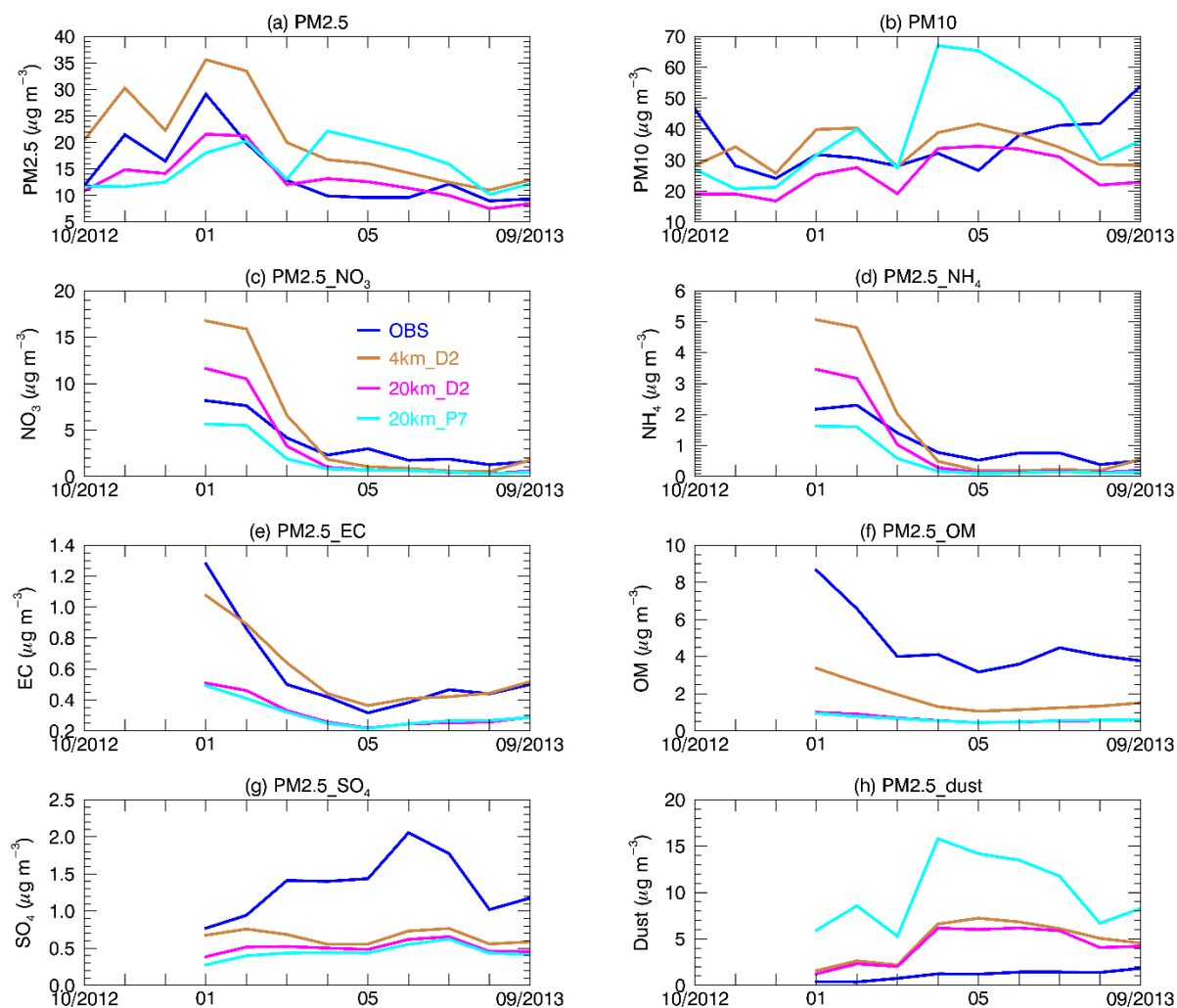
932

933   Supplementary Figure 5. Aerosol mass (μg m⁻³) for different species from EPA CSN (OBS), the

934   4km_D2, 20km_D2 and 20km_P7 simulations at Modesto, CA.
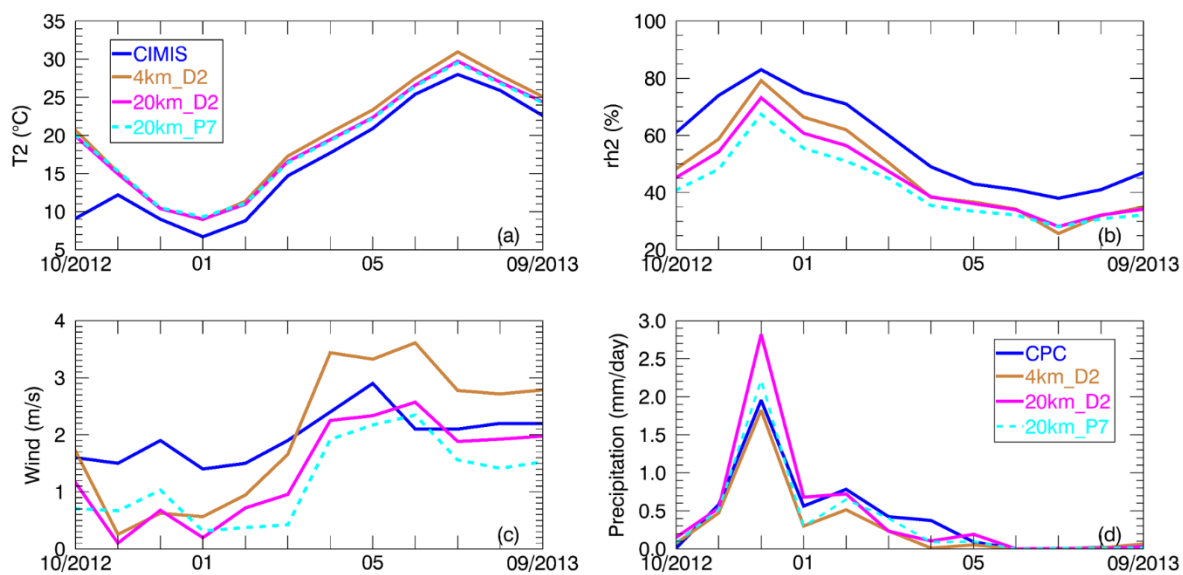
935

936 Supplementary Figure 6. Monthly mean of (a) 2-m temperature (°C); (b) 2-m relative humidity

937 (%); (c) 10-m wind speed (m/s); (d) precipitation (mm/day) at Fresno, CA. The 20km (not shown)

938 run is similar to the 20km_D2 run while the 4km (not shown) run is similar to the 4km_D2 run.
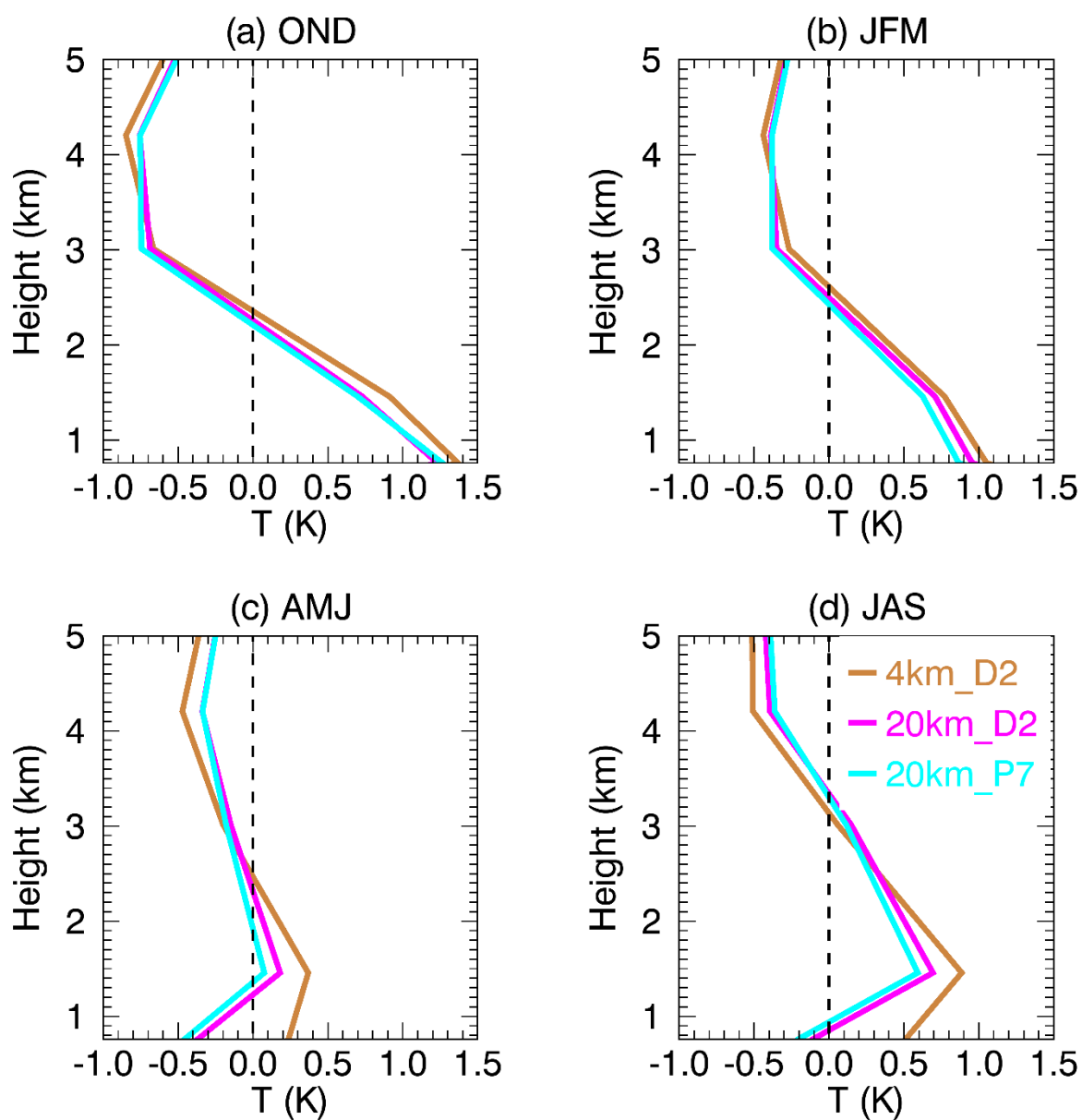
939

940 Supplementary Figure 7. Vertical profile of seasonal mean temperature (K) bias in the WRF-Chem

941 simulations comparing to AIRS. The 20km run (not shown) is similar to the 20km_D2 run while

942 the 4km run (not shown) is similar to the 4km_D2 run.
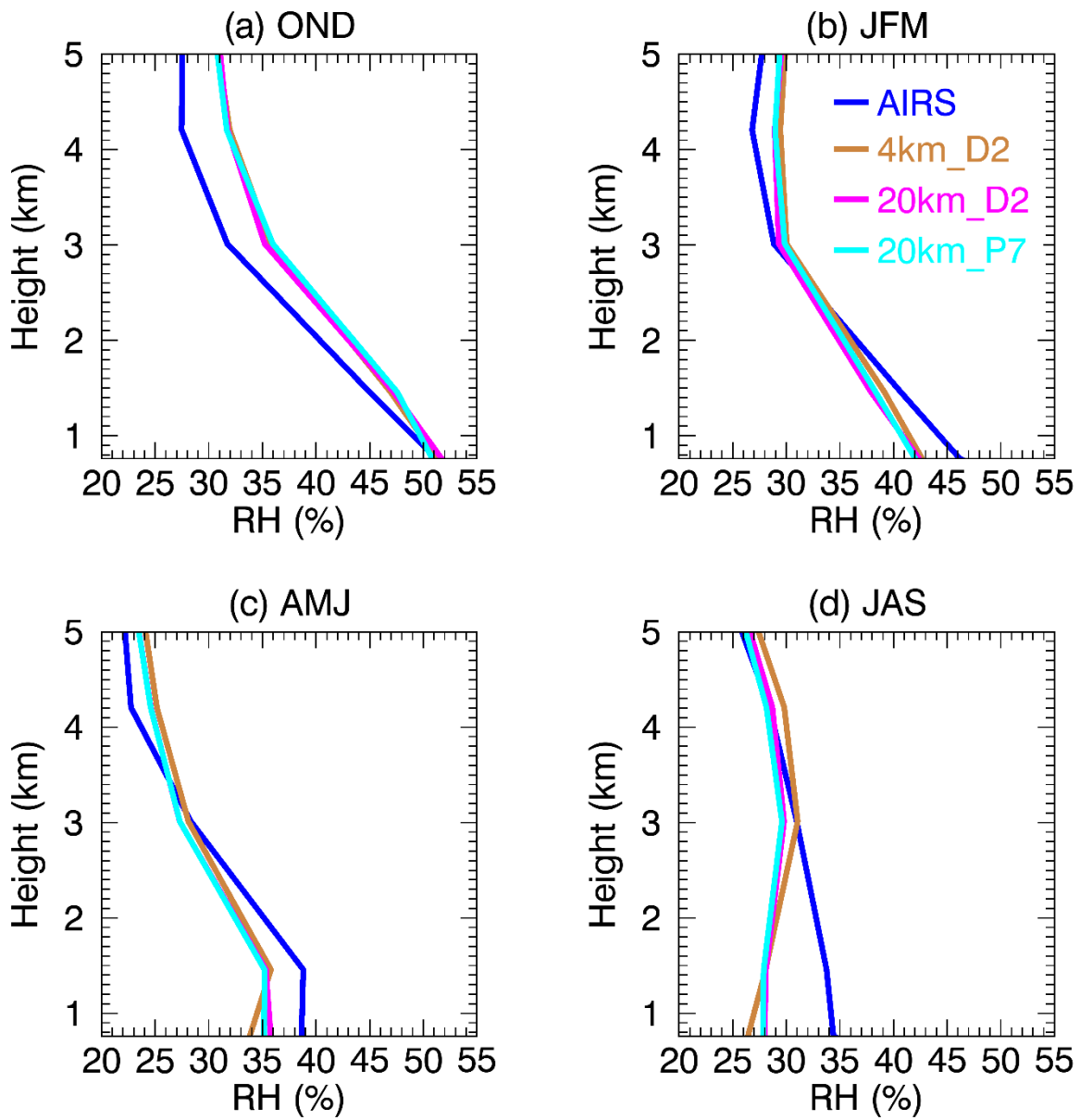
943

944 Supplementary Figure 8. Vertical profile of seasonal mean relative humidity (%) in the WRF-Chem

945 simulations comparing to AIRS. The 20km run (not shown) is similar to the 20km_D2 run while

946 the 4km run (not shown) is similar to the 4km_D2 run.